Application of a mechanistic single droplet drying model to spray drying process at different scales

Master's thesis in Master Programme: Innovative and sustainable chemical engineering

KARL SJÖBERG

DEPARTMENT OF CHEMISTRY AND CHEMICAL ENGINEERING

CHALMERS UNIVERSITY OF TECHNOLOGY
Gothenburg, Sweden 2023
www.chalmers.se

Master's thesis 2023

Application of a mechanistic single droplet drying model to spray drying process at different scales

KARL SJÖBERG

CHALMERS
UNIVERSITY OF TECHNOLOGY

Department of Chemistry and Chemical Engineering
Chalmers University of Technology
Gothenburg, Sweden 2023

Application of a mechanistic single droplet drying model
to spray drying process at different scales

KARL SJÖBERG

Examiner
Creaser, Derek
Professor, Chemistry and Chemical Engineering, Chemical Reaction Engineering

Supervisors
Nguyen, Duy
Senior scientist MAN, AstraZeneca
Niklasson Björn, Ingela
Associate principal scientist GMD, AstraZeneca
Martin de Juan, Luis
Associate principal scientist GMD, AstraZeneca

Master's Thesis 2023
Department of Chemical engineering
Division of Chemistry and Chemical engineering
Chalmers University of Technology
SE-412 96 Gothenburg
Telephone +46 31 772 1000

Typeset in LaTeX
Printed by Chalmers Reproservice
Gothenburg, Sweden 2023

Abstract

Spray drying is a rapid drying process which utilizes direct heating via convection to form solid powder material of certain desired properties, e.g. specific size distributions from liquid/suspensions. Within the pharmaceutical field, one example of where spray drying is used is to create inhalable powders.

There is a general need to use more modelling tools to speed up product development also in the pharmaceutical area. One example of modelling software currently used is the flowsheeting tool - gPROMS (general PROcess Modelling System made by Siemens Process Systems Engineering), that can be used to build digital twins. The rationale of building a digital twin within gPROMS was its abilities to serve as a tool for in-depth analysis and process control even for an in-experienced user. The purpose of this work was to build a key component of the spray dryer to add more advanced functionality relevant for spray drying within the inhalation area.

The major results show excellent predictions to describe the:
Impact of critical concentration on shell formation
Impact of diffusion coefficient on shell formation
Large water droplet drying

Keywords: Spray drying, Particle formation, Modelling, Diffusion, Parameter estimation

Acknowledgements

I would like to thank my supervisors at AstraZeneca for the help during the thesis. My friends and family.

Karl, Göteborg, August 2023

List of Acronyms

API	Active pharmaceutical ingredient
AZ	AstraZeneca
CDC	Characteristic drying curve
CDF	Cumulative lognormal distribution
CFD	Computational fluid dynamics
CSTR	Continously stirred flow reactor
DOE	Design of experiments
DPI	Dry powder inhaler
DS	Double safety margin
DSD	Droplet size distribution
ESCA	Electron spectroscopy for chemical analysis
GCI	Grid convergence index
GMP	Good manufacturing practice
gPROMS	general PROcess Modelling System
LPP	Large porous particle
ML	Maximum likelihood
MLE	Maximum likelihhod estimator
NRMSE	Normalized root mean square error
PSD	Particle size distribution
REA	Reaction engineering approach
RMSE	Root mean square error
SEM	Scanning electron microscope
SSA	Specific surface area
VFL	'Vehring, Foss, Lechuga' model

Nomenclature

Parameters

M_w	Molecular weight water
M_g	Molecular weight drying gas
R	Universal gas constant or normalized radial coordinate
k_b	Stefan-Boltzmann constant
R_A	Molecular radius
F_a	Factor of safety
r	Grid refinement ratio

Variables

d_p	Particle diameter
d_D	Droplet diameter
C_f	Initial solute concentration
ρ_p	Particle density
ρ_l	Solvent density
P	Total pressure
τ_D	Maximum drying time
τ_{sat}	Time to reach saturation at droplet surface
κ	Constant drying rate
T	Temperature
T_g	Glass transition temperature
X	Dry moisture content
x	Wet moisture content
Y	Absolute humidity

$\dot{m}_D$	Evaporated moisture
ϕ	Relative humidity or characteristic moisture content
D	Diffusion coefficient
E	Energy transfer or surface enrichment
ΔH_{vap}	Enthalphy of vaporization
ΔG_{mix}	Gibbs free energy
N	Number of moles
χ	Interaction parameter
Φ	Volume fraction
h	Heat convective transfer coefficient
k_c	Mass convective transfer coefficient
Re	Reynold
Ra	Rayleigh
Sh	Sheerwood
Nu	Nusselt
Pe	Peclet
$\hat{N}_v$	Constant drying rate
N_V	Falling drying rate
A	Area
Ψ	Fractionality coefficient
C	Concentration
S	Initial saturation
m	Droplet mass
y_i	Experimental value
$\hat{y}_i$	Predicted value
L	Characteristic length
q	Heat flux
Q	Energy transfer
θ	Number of droplets per droplet size
U	Heat loss constant
C_p	Specific heat capacity for constant pressure
μ	Mean
σ	Variance
$\dot{V}$	Volume flow rate

h_{body}	Spray dryer body heat loss constant
h_{pipe}	Spray dryer pipe heat loss constant

Contents

List of Figures

List of Tables

1

Introduction

In the pharmaceutical industry spray drying is a common unit operation. Spray drying is used to produce dry powder from liquified feedstocks containing active pharmaceutical ingredients (API), exipients (bearers and/or stabilizers of the API) and solvent(s). Spray dried powders are used in a wide range of medical treatments by different forms of administration, such as oral, nasal and trans-dermal. In pulmonary therapeutics, spray dried powders can be administered via inhalation as aerosols using dry powder inhalers (DPI) [1]. One example of DPI use is to acutely relieve or prevent symptoms caused by asthma, which is a chronic lung disease responsible for occasional breathing difficulties [2, 3].

The particles constituting dry powders for inhalation may vary in size, but are all required to be within a specific size range (most often below 5 μm) in order to reach down through the airways to the target sites within the lungs, e.g. alveolar. In addition to size, their physical properties; geometrical size and morphology are crucial for effective and safe treatment. These attributes highly affect the stabilisation of active components, systematic delivery by transport and targeting as well as drug release modulation. Particle design using process parameters and formulation material properties provides means to steer particle formation to attain more advanced drug delivery systems which opens up for more sophisticated therapeutics [1, 4].

There is a general need to enhance understanding and implement models of particle formation that can predict what occurs before and after shell formation during spray drying. By using model simulations ('digital twins') as process control systems the real life spray drying operation can be assessed and optimized to produce particles of the correct specifications.

The overarching goals of building a digital twin of the spray drying process is to firstly acquire simulation information that possibly could add onto the guarantee that the product is of good manufacturing practice (GMP). This means that particles are made in a controlled sterile environments and they are both safe and works reliably to treat drug recipients, the patients. In addition by acquiring in-depth knowledge of particle formation the particle design could be tailored during operation with formulations and process parameters. Also particles could be optimised to reduce the amount of costly API used, possibly decreasing ecological strain and making pharmaceuticals derived from spray dried particles more accessible.

1.1 Spray drying operation

Spray drying is used to directly create solid small particle size matter from liquid formulations with a specific size distribution in a continuous and fast manner. The spray dryer consists of three major parts. Figure 1.1 visualizes the atomizer, drying chamber and cyclone which respective responsibility are discretization of liquid formulation into droplets, drying of droplets into particles and collection of particles.

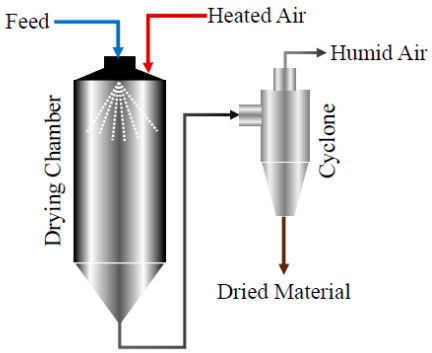

Figure 1.1: Schematic of spray drying unit, [5].

The spray dryer used in pharmaceutical production operates co-currently which decrease unwanted re-circulation and allow for processing of temperature sensitive material reducing risk of thermal degradation. In addition, the uniformity of properties of the particles created enables easy handling, solid configuration and enhanced product stability [4]. However, this type of drying process is usually highly energy-intensive as the energy needed for evaporation of solvents is supplied thermally by convection [6]. Also as the formulation is in liquid phase the evaporative heat load is high [7].

1.1.1 Atomizer

The atomizer functions to discritize continous homogenous formulation liquid flow into droplets. The choice of atomizer technique and driving force depends on product specification. For the target particle size of inhalation drugs 1 - 5 μm the 'pressure' or 'two fluid' nozzle are the most commonly used, creating initial droplet sizes below 10 μm [4, 8, 9]. Figure 1.2 depicts how the two fluid nozzle operates with co-currently fed liquid solution and atomization gas.

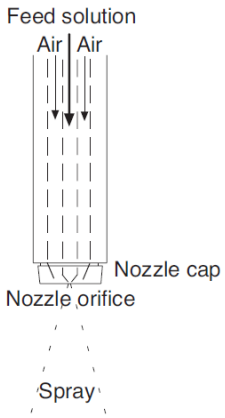

Figure 1.2: Two fluid nozzle, [4].

The driving force of the two fluid nozzle is the relative velocity between the liquid formulation and the atomization gas, which is set in combination by material and gas flow and geometry of the nozzle. The carrier gas as well as drying gas used in pharmaceutical industry is nitrogen [8, 9]. Size of droplets formed is highly dependent on the precursor material properties, such as density ρ, surface tension σ, viscosity μ, atomizer type, size of feed, atomizer and drying gas material flows. The droplet size d_D is usually described from semi-empirical correlations [4, 8, 10]. With conditions of assuming no further cleavage or droplet coalescence after discretization within the drying chamber the atomizer performance i.e. the droplet size and size distribution can be used to approximate the final particle size and size distribution [9, 11]. From process conditions and initial solute concentration the final particle size and initial droplet size has been shown to follow a linear relationship [4].

$$d_p = \sqrt[3]{\frac{C_f}{\rho_p}} d_D \tag{1.1}$$

With d_p and d_D are the particle and droplet size, respectively. C_f the initial solute concentration and ρ_p the particle density [1].
The atomizer can also be characterized by the size distribution of droplets produced. Size distribution is for practical reasons explained in quantiles that describes how many droplets which size is below a specific size. Cumulative size distribution is defined as

$$F(d_D) = \int_0^{d_D} f(t)dt \tag{1.2}$$

Where the quantile $F(d_D)$ gives the amount of droplet as a fraction, that has the diameter size smaller than d_D. For eg. the quantile D50 corresponds to the size value which 50 % of the droplet size data are less than.

1.1.2 Drying chamber

The solvents' primary function is to homogenously mix and solubilize the ingredients in the formulation step. To create solid amorphous particles the solvent(s) are

to be evaporated away. How quickly this occur depends on the driving force of evaporation,

$$\Delta P_i = P_{surf,i} - P_{gas,i} \tag{1.3}$$

which is the difference of vapor pressure $P_{surf,i}$ at the droplet surface and gas partial pressure $P_{gas,i}$ of the solvent component i [8].
In spray dryers direct heating via convection is employed by its simplicity to regulate temperature. When drying hygroscopic material (material with moisture retaining capacity) such as the solid in the formulation, the moisture content in the solid material decreases. Figure 1.3 shows how a gas acts as a drying medium.

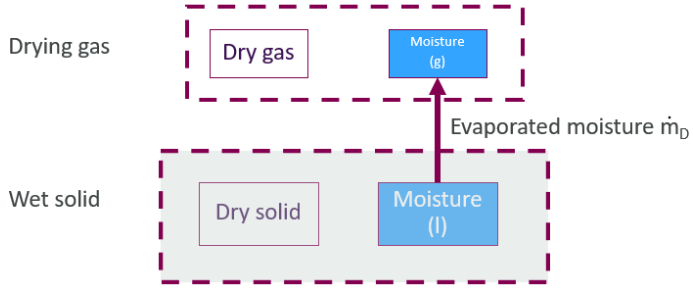

Figure 1.3: Schematic of drying - with gas as a drying medium

The moisture to solid ratio in dry solid basis is defined as

$$X = \frac{m_{wet,s} - m_s}{m_s} = \frac{\text{kg solvent (l)}}{\text{kg dry solid (s)}} \tag{1.4}$$

Where m_s is the dry solid, $m_{wet,s}$ is the wet solid accounting for both the mass of dry solid and the moisture. Simultaneously the evaporated solvent increases the humidity of the drying gas, with the absolute humidity of drying gas defined as

$$Y = \frac{m_w}{m_g} = \frac{M_w}{M_g}\frac{P_w}{P - P_w} = \frac{\text{kg solvent (g)}}{\text{kg dry gas (g)}} \tag{1.5}$$

Where m_w and m_g is the moisture in the gas and mass of dry gas respectively. M_w and M_g are their respective molecular weights. P_w is the partial pressure of the solvent and P is the total pressure. Using a macroscopic balance of the mass entering and leaving the dryer with the corresponding absolute humidities the solvent evaporated into the drying and atomizer gas can thus be described as

$$\dot{m}_s(X_{in} - X_{out}) = \dot{m}_G(Y_{out} - Y_{in}) = \dot{m}_{solvent,evap} = \dot{m}_D \tag{1.6}$$

The relative humidity ϕ is defined as the ratio of the solvent pressure to the solvent saturation pressure at the temperature and total pressure operating conditions. The relative humidity is useful for quantifying the drying capacity of the drying gas.

$$\phi = \frac{P_w}{P_{w,sat}} \tag{1.7}$$

Rewriting the equation 1.5 into

$$P_w = \frac{PY}{Y + \frac{M_w}{M_G}} = \left[D = \frac{M_w}{M_G}\right] = \frac{PY}{Y + D} \tag{1.8}$$

Rewriting partial vapor pressure and saturation vapor pressure with equation 1.8, the relaitve humidity can be approximated as

$$\phi = \frac{(Y_s + D)Y}{(Y + D)Y_s} = \left[\text{if D»Y}\right] \approx \frac{Y}{Y_s} \tag{1.9}$$

Where Y_s is the saturation absolute humidity at as specific temperature and total pressure [12].

1.1.3 Drying regimes

The drying pathway from droplet to particle is illustrated in figure 1.4, starting from droplet, to wet particle, to dry particle. Due to distinct difference in drying kinetics, the drying of droplets is usually split into two stages, a constant drying rate and a falling drying rate. The constant drying rate is controlled by both external mass and heat transfer limitations, whereas the falling drying rate is controlled by internal mass transfer.

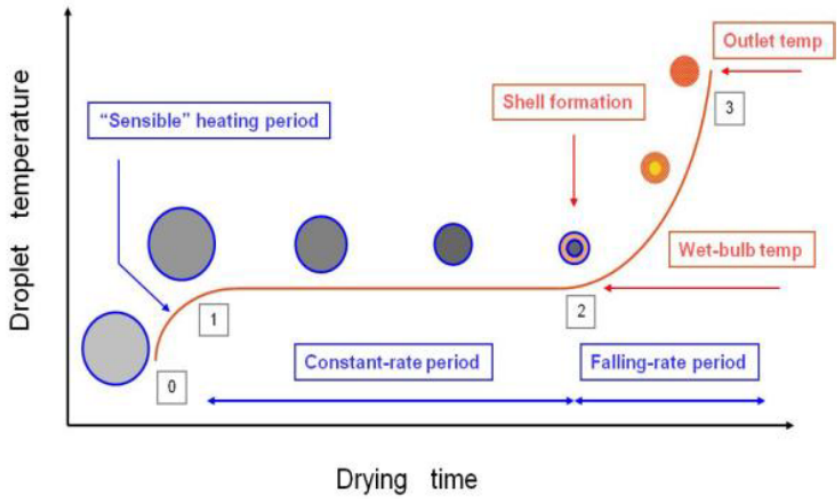

Figure 1.4: Schematic of droplet drying history and morphological changes, [13].

As the droplet (consisting of dissolved solids and solvent) is first introduced to the hot drying gas sensible heating of the droplet occurs until it reaches wet bulb temperature. At the wet bulb temperature evaporation takes place at a constant rate dictated by the convective heat transport to the droplet and the external moisture content in the gas. Within this stage the droplet surface is fully saturated by solvent exhibiting pure solvent properties. During this period the droplet decreases in size corresponding to the amount of mass leaving by evaporation. After some time the concentrations of solutes at the droplet surface reaches a critical point where a

skin/crust is formed. As the crust successively increases in width the location of evaporation recede toward the interior crust liquid-solid interface, where the crust permeability of the solvent vapour diffusion effectively reduces the rate of mass transport towards the outer surface. Within this falling rate period the evaporation rate becomes mass transport limited by internal diffusion. At this stage the particle and leftover solvent heats up, until it reaches the outlet temperature of the spray drying vessel [14].

1.1.4 Drying time

The wet droplet is in contact with hot drying gas as it enters the vessel from the atomizer. Roughly at 10^{-2} s crust formation occurs, making the droplet lifetime very short. The total residence time within the spray dryer body of a droplet/particle is on the magnitude of 10^{-1} to 10 s [4, 15]. Figure 1.5 reflects upon the physical evolution from droplet to particle.

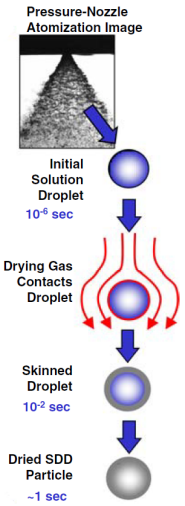

Figure 1.5: Physical situation of the spray drying process , [15].

To retrieve completely dried particles at the end of the dryer, the residence time must be atleast the same or exceed the maximum drying time τ_D which can be approximated from a constant drying rate κ and initial droplet diameter known as the 'd^2 law' ,

$$\tau_D = \frac{d_D^2}{\kappa} \tag{1.10}$$

[1, 8, 11].

Figure 1.6 relates the drying profile of a droplet to particle and temperature with the characteristic drying times.

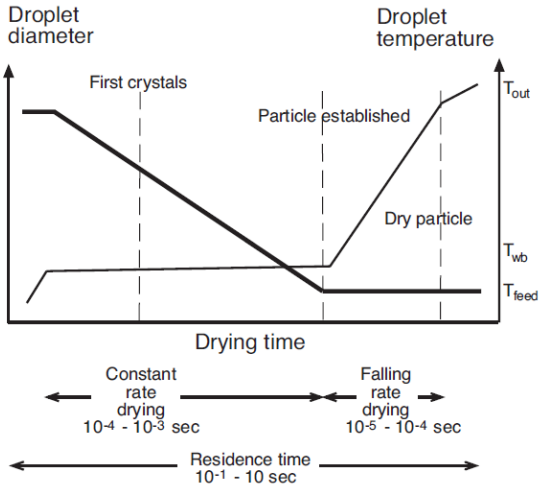

Figure 1.6: Schematic drying profiles showing the dynamics of size and temperature of the drying droplets of the spray dryer, [4].

The aim of drying inside the spray dyer is to remove solvent by traversing through the drying regions as quickly as possible to get to the point where the $T_g > T_{out}$. This is to reduce the mobility of API and the risk of phase separation by highly viscous glass creation below T_g. Sometimes this rapid temperature shift is referred to as 'quenching' [8].

1.2 Particle morphology

This section describe some of the most important relationships between process parameters and feedstock composition to particle morphology.

Process parameters and feedstock composition affects final particle properties such as size, density, composition and morphology. These parameters in turn affect final product functional properties such as stability and administration in terms of flowability, dispersibility, deposition and solubility. Controlling the product properties by particle engineering can therefore give enhanced performance [1, 7, 11].

Utilizing spray drying with aerosol-assisted self-assembly technique particles with nanometer properties on the macroscale can be made [10]. Another example is the creation of large porous particles (LPP) which are found to be dispersing well from dry powder inhalers and have efficient deep deposition inside the lung, see figure 1.7.

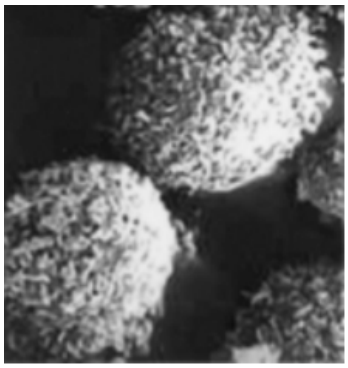

Figure 1.7: Electron micrograph of a low density porous particles, with size known to be less than 10 μm, [16].

With relatively large geometric diameter combined with low density, the aerodynamic diameter is still in the respirable size range, see equation 1.1 [8, 16].

1.2.1 Formulation

Solute concentrations within the formulation impacts both the commence of shell formation and its structural stability (flexibility). The particles structural stability depends on shell rigidness and thickness. Figure 1.8 shows that increasing solute concentrations (solute loading) slightly in the dilute domain has large impact on particle size (as higher solid content will lead to much quicker shell formation), wheras at moderate or high concentrations the change is minor [4, 9, 17].

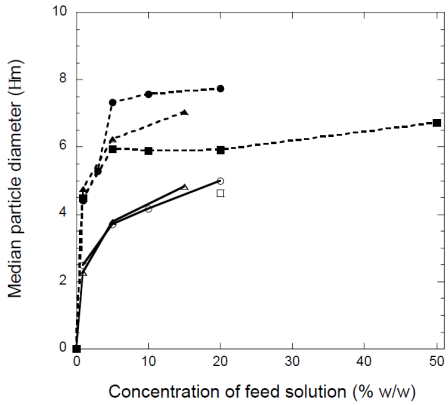

Figure 1.8: Spray dried lactose (circle), mannitol (triangle), sucrose (square) from two different droplet size (open=small, filled=large), [4].

An analogous discovery was made in a study of Würster bed coating, where the coating liquid formulation in terms of the initial solid mass impacts both the coatings ring height and the shape [18].

1.2.2 Surface active components

Solutes and excipients could be divided into two subdomains, surface active or non-active. Surface active molecules have an affinity to move to the droplet surface and preferentially adsorb to the gas-liquid interface irrespective of the solubility of components inside the droplet. Wheras non-active components could be said to solely be steered by diffusion and internal convection. Surface active components are thus likely shell formers, as what reaches the surface most probably stays there. However, it is unclear if secondary shell formers (component which have higher surface affinity than the primary shell former) are able to push away the primary in the short droplet life-time. Therefore, it is important to know if the constituting components in the formulation exhibit these kinds of properties as they will affect the particle morphology. In addition, for formulations containing surface active protein API, there is risk of loosing much of effective API. As protein reaching the surface unfold from their natural state, entangle, become denaturated and create a hard unsoluble shell [4].
From spray drying studies of milk, it has been postulated that the surface active protein could be restrained by a quicker shell formation brought by higher drying temperature [19]. There are also potential benefits of using surface active components to trap API inside particle sub- or shell domain. Another advantage with surface active components would be their abilities to enhance product delivery. One example is trileucine (a surface active protein with low solubility) which has been found to coat the particle with a rougher surface increasing dispersibility [1]. Although, examining experimental results and post-processing information of surface active components and shell formers is hard. Common analysis methods like Electron spectroscopy for chemical analysis (ESCA) has low penetration depth (about 5-10 nm) which makes it difficult to distinguish between a shell or potential coat [20, 21].

1.2.3 Solubility

It has been shown in spray drying of milk that larger molecules oftentimes follow a 'solubility effect'. The solubility effect essentially say that the molecular size is to explain the effects of low solubility, diffusivity and surface activity [22]. From a pharmaceutical standpoint the theory of diffusional motion to predict particle formation is said to be lacking. Pharmaceutical formulations can include larger molecules like proteins, polymers and carbohydrates which lead to slow diffusional movement and particles which become hollow. Solutes or exipients with low solubility may also create low density particles, as they reach saturation, precipitate (phase separate) and accumulate at the surface [23].

1.2.4 Drying temperature

Temperature as a process parameter has great impact on the creation of particle morphology and its subsequent properties, e.g. dispersibility. Some examples of particle morphologies are shriveled, buckled or inflated particles. Qualitatively described, 'slow' low temperature drying results in buckled particles with high density,

whilst 'fast' high temperature drying lead to spherical and smooth particles, inflated or if the temperature is high enough ruptured 'puffed'. See figure 1.9 which show SEM images of inflated and buckled particles.

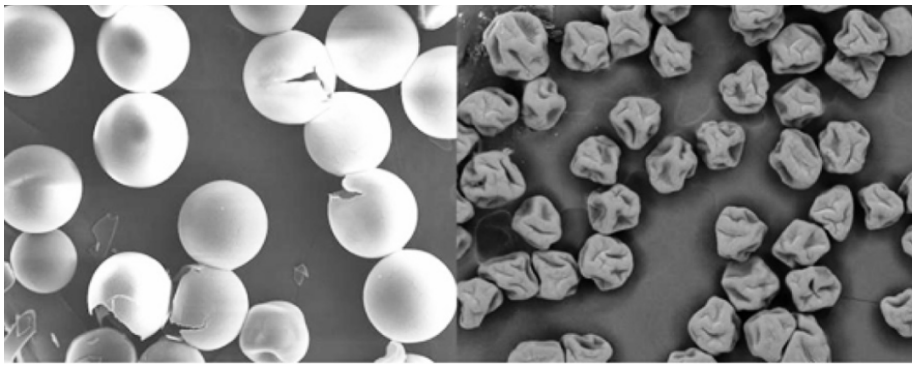

Figure 1.9: SEM images of inflated, ruptured 'puffed' particles dried from 33 wt% fresh skim milk concentrate at 180 °C and buckled particles dried from 33 wt% skim milk concentrate at 180 °C, [17].

Drying temperature affects how quickly drying is progressed and residual moisture content. Both the temperature and the moisture content contributes to the mobility of components within the particle. Above a certain composition range dependent temperature called the glass transition temperature T_g the material softens, increasing the mobility of components. Figure 1.10 show moisture content and temperature trajectories of spray drying.

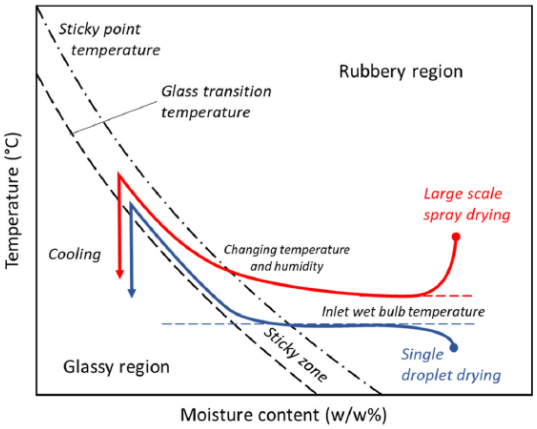

Figure 1.10: Schematic representation of the change in moisture content and temperature of the surface of a droplet during drying at either single droplet or large spray drying scale, [24].

In addition residual moisture content acts as a plasticizer within solid amorphous material lowering the T_g. Increased mobility can lead to decreased chemical and physical stability of final product, such as phase separation and crystallization [8, 19].
High drying temperature can also have other effects as shown from Würster bed

coating, where the coating of a glass bead gave smoother surface coverage when the temperature was above T_g [18].
Results from CFD studies of the spray drying chamber show in figure 1.11 that gas temperature is high in the vicinity to the atomizer nozzle, however not too far away the gas temperature rapidly changes to the outlet temperature.

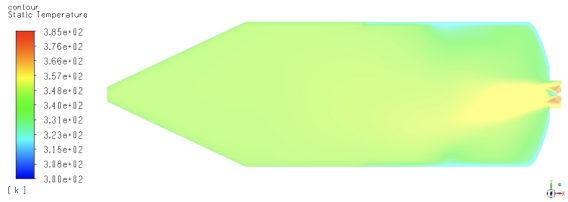

Figure 1.11: Static temperature contour plot shown on a sectional plane of Anhydro MicraSpray 35 (MS35), (picture is oriented horizontally while the spray setup is vertical) [25]

With regards to the average residence time of a droplet to particle and the drying gas temperature profile within the drying vessel it is clear that the majority of the droplet-/particles' time inside the dryer is spent in gas which temperature is close to the outlet temperature.

1.2.5 Particle inflation

The phenomena of particle inflation affects product attributes by increased overall size, area and decreased density. Particle inflation occurs at high temperature drying with low initial solid concentration. In this scenario a flexible shell is formed quickly as particle temperature increases towards outlet temperature. Depending on the volatility of the solvent the temperature may be high enough for the solvent to boil inside, increasing pressure exerted outward and inflating the particle [9].
Furthermore, high temperature drying could induce large enough pressure difference between the interior and exterior of particle such that tensile drying stress cause the particle shell to rupture, creating a 'puffed' particle [12, 26].
In a study of drying large milk droplets (mm scale) which are much larger than inhalation particle sizes, results suspect to show inflation. High temperature fast evaporation was reported to create smooth spherical hard shells prone to resist deflation. Authors postulate that the shell is flexible enough to expand at the initially high temperature and then at lower temperatures mechanically strong enough to not deflate. Correspondingly the fact that particles dried under 'cold' lower temperature outlet conditions has propensity to deflate or/and shrivel as the shell is not sturdy enough [19].
However, the effect of higher drying temperature resulting in inflation could be deceptive and misleading. Particles examined which differ significantly in size, thought to be inflated could just be agglomerated particles. This could be explained by too high temperature directly at the spray dryer nozzle, forming agglomerations of colliding droplets as drying occurred faster than the full development of the spray at the nozzle [9]. This phenomena is commonly referred to as 'stringing'. Also, it is unclear whether microdroplets do inflate during drying. For it to happen the particle

surface must increase diffusional resistance such that particle temperature exceeds the boiling point of the wet core. In addition the bubble has to have sufficient time to nucleate and exert outward pressure [1, 4].

1.2.6 Buckling

Buckling is a common phenomena for suspension formulations [27]. It is attributed to the local particle density elevations that occur when the surface recede inwards from evaporative drying. As the surface shrinks, the shell gets thicker and particles within the shell are packed more closely, stabilizing the shell from further contraction by their electrostatic repulsive forces. However, the evaporation of solvent does not stop and is dependent on the permiability of the shell. Whilst the particle looses solvent pressure difference to the surroundings become larger, creating a compressive capillary stress on the shell. Pushing the particles inward and pulling the solvent outward. When the stress overcomes the electrostatic force, the shell buckles from elastoplastic deformation [28].

In an article, [17], assessing the morphology of milk powder made by spray drying results proposes that the assumption of isotropic perfect shrinkage (volume of droplet is reduced by the same amount as evaporated liquid) correlates well with the shrinkage in the form of buckling that the particles experience.

1.3 Predicting stability and phase separation

The purpose of spray drying homogeneous solution is to form a thermodynamically stable amorphous system. This is done either by utilizing a low drug loading or fast drying kinetics with fast extinguishing. The Flory Huggins model can be used to predict the stability or phase separation of a system containing API and polymer with Gibbs free energy, ΔG_{mix}, see figure 1.12.

$$\Delta G_{mix} = RT\left(N_A ln(\Phi_A) + N_B ln(\Phi_B) + \chi N_A \Phi_A \Phi_B\right) \tag{1.11}$$

Where Φ is the volume fraction, N the number of moles, χ the interaction parameter of the polymer and the drug. ΔG_{mix} contains both an entropic and enthalpic term of mixing. The entropy of mixing is always a negative term as mixing is favourable.

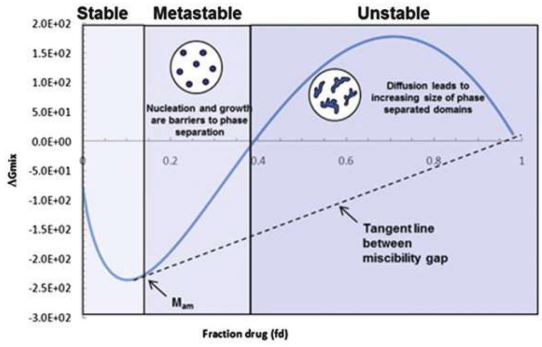

Figure 1.12: Simple binary Flory-Huggins description of thermodynamic versus kinetic situations in amorphous dispersions, [8].

If the condition of $\Delta G_{mix} < 0$ is held over all compositions, and there is only a single minimum of the curve, the system or the mixture is fully miscible. If however, there are two minima there will be a thermodynamic force which drives the system into spontaneous amorphous phase separation. Increased drug loading increases ΔG_{mix}, however it is possible to create meta-stable state if the subsequent cooling of the system is fast enough. The mobility decreases with the temperature making the amorphous system trapped kinetically.
A system will however phase separate over time creating heterogenous system of amorphously or crystalline pure domains, which risks the performance of the pharmaceutical product. In order to keep the thermodynamic time of phase separation higher than the relevant pharmaceutical time-frame and to increase the long term stability of the product the glass transition temperature is chosen to be high in comparison to ambient temperatures, to substantially decrease mobility [8].

1.4 Thermodynamic operating space and scale-up strategies

Retrieving experimental data for a basis of scale-up decision making is hard by the non-equilibrium nature that droplets experience during rapid spray drying process. It is also difficult to envision how process parameters and product properties relate solely on a statistical design of experiment (DOE) approach. Instead it is preferable to devise a thermodynamic operating and design space of the spray dryer theoretically with fundamental physical principles governing the drying process.
Defining the spray drying vessel geometrical domain as the macroscopic control volume and using zero-dimensional mass and heat balances it is possible to determine key process parameters, input and output conditions without performing experiments [8, 15].
Assuming conservation of mass, energy and a full adiabatic system, the amount of energy necessary for evaporating the entirety of the solvent is described as

$$\Delta E = m_{feed}(1 - X_{solid})\Delta H_{Vap} \tag{1.12}$$

Wheras the energy transfer for the drying gas inside the vessel is

$$\Delta E = m_{gas} C_{p,gas} (T_{in} - T_{out}) \tag{1.13}$$

By equating equation 1.12 and 1.13, T_{out} is determined as

$$T_{out} = T_{in} - \frac{m_{feed}(1 - X_{solid})\Delta H_{Vap}}{m_{gas} C_{p,gas}} \tag{1.14}$$

From zero-dimensional balances using the process parameters T_{in}, m_{feed}, m_{gas}, X_{solid} and absolute pressure within the spray dryer $P_{chamber}$ constraints of the process independent of scale can be developed. In addition, even without knowing the exact geometry, the knowledge on how parameters affects the process enables transition between scales. However, as heat losses are dependent on wall buildup and vessel material properties these must be experimentally determined.
For the creation of solid amorphous particles it is important to control the left-over solvent inside the material as it affects the mobility of the API. The solvent can possibly reduce the glass transition temperature T_g to become lower than T_{out} and increase the risk of phase separation and crystallisation. One indicator of the left-over solvent is the relative humidity ϕ at the outlet [8, 29]. The value of ϕ attained from the smaller scale operation or from experiments could be transferred as a cautionary criteria for the larger scale [29].
A multivariate graph of these variables in coordination with process equipment and formulation limitations generates a theoretical landscape of both the operating and design space. Some examples of settings that are desired to have efficient operation, throughput and quality: To dry quickly T_{in} should be as high as possible without causing stringing or damaging the product, $\dot{m}_{feed}$ as concentrated as possible to reduce energy demand, T_{out} to be below T_g to decrease mobility and ϕ to be low enough to avoid sticky particles causing wall buildup and loss of material [15, 30].

1.5 Particle engineering

Today, the main issues of particle engineering is to use the initial formulation together with process parameters to predict the internal radial distribution of solutes, shell formation and final particle structure, (morphology) [22, 31].

1.5.1 - Within the lab

There exists many types of experimental single droplet drying techniques on the lab scale that soughts to provide pathways to both qualitatively and quantitatively describe the drying kinetics and evolution of particle morphology. However, the weakness with these methods are that they often employ large droplet sizes and different drying settings often not accounting for phenomena occuring within real industrial production. The experiments commonly use idealization of flows, neglects interactions between droplets, particles and walls. Predictions based upon experiments may also fail due to inaccurate data recordings caused by fast drying with non-equilibrium and by the variability of feed parameters during operation.

Furthermore, inhalation medicine most often consist of multicomponent solutions. Where each component has their own specific material properties. Blending together material in a solution can cause material properties and interactions to change. Therefore during drying droplets may experience separation of components by their differences in diffusion, solubility, hydrophobicity, amphiphilicity and/or density. These can all be seen as driving forces that cause the component distribution within a droplet/particle to change [31].

1.5.2 - With models

Spray drying is rapid process which entails simultaneous multiphase transport phenomena between gas, liquid and solid. Each phase also experience internal and external exchange of heat and mass. The drying process progresses quickly which causes the material within the spray dryer to experience non-equilibrium conditions. For this reason it is hard to evaluate the real physical phenomena solely with experiments occurring at equilibrium or by non-invasive probing [1, 4, 32].

With models based on mechanistic/first principles it is possible to build knowledge outside the lab. The information retrieved from simulations may give greater insight from a process engineering perspective where it could simplify and optimise operational control to be on par with predicted outcome, such as particle properties, size and morphology.

Still, model equations describing spray drying need to be validated against experimental results. Either by formulations based on the real API formulation, using small quantities of API or by the use of a placebo, which has no therapeutic value. Nevertheless, the use of placebo is motivated by the capability of specific constituents like polymers to create near resemblance of the real formulation properties. By using a large mass fraction of a single component within the placebo the fluid properties, shell formation and drying phenomena can be dictated by the molecular weight and the polymer propensity to create a film [15].

1.6 gProms - digital process twin technology

gPROMS (general PROcess Modelling System made by Siemens Process Systems Engineering) is a flowsheeting tool made for process engineering e.g. in areas of research and process control. It utilizes a programming language in which mathematical models are constructed and used to describe physical phenomena. This allow for digital twin construction of real processes with several unit operations. It is user-friendly, making use possible for people with different backgrounds even with no prior programming experience. The language is mostly declarative, which means that the equations describing the system can be written as they are. Models are written in a generic way, the specific situation to be simulated is performed within dynamic simulation activity and is done by linking the model(s) with a or several process(es). gPROMS also has strong model validation tools e.g. parameter estimation to fit model parameters to experimental data.

1.7 Aim

The general aim of the thesis was to implement a spray drying model which could be coupled to an already built process engineering model library, enabling digital twin construction of the entire process unit. This model would integrate some new features concerning particle formation, complementing the process library.

1.8 Objectives and workflow

The aim was divided into several parts. A thorough literature review was undertaken to acquire knowledge about single droplet drying models explaining before and after shell formation in detail, as well as spray drying models of flows, approximated as a continously stirred tank reactor (CSTR) or plug flow reactor (PFR). Furthermore single droplet drying and spray drying 'flow' models from the literature review were evaluated in a feasibility study to determine their comparative benefits and drawbacks to define a suitable modelling approach. One single droplet- and one spray drying model was chosen to be combined in an overall model to be implemented. This combined model was coupled as a unit in the programming and flowsheeting software 'gPROMS' describing heat and mass transfer inside the spray dryer aswell as heat losses derived from parameter estimations of experimental results.

Critical parameters such as diffusion coefficients and critical concentrations of formulation components were looked upon to discover any possibility to predict shell formation of particles from droplets within the spray dryer. Validation and discussion of the results acquired as well as future outlooks was presented.

1.9 Out of scope

The thesis is only related to spray drying from dry powder perspective. It only concerns topics of particle drying, spray drying flow regime cases inside the vessel, particle shell formation, particle and shell morphology.

As a spray dryer is a multicomponent unit operator the report does not in depth consider parts such as the atomizer, particle separation with cyclone, condensor or recirculation of drying gas.

2

Theory

2.1 Droplet drying models

2.1.1 Lumped models

Lumped models assume spatial uniformity of droplet/particle system properties. Their primary modelling quality is their description of the secondary drying stage kinetics within the droplet/particle scale. They do not handle any smaller subsystems below particle scale. The lumped models rely on experimental data for approximating formulation material properties during the drying process. In addition they use semi-emperical correlations to determine heat and mass convective transfer coefficients h and k_c from dimensionless numbers Nusselt (Nu) and Sherwood (Sh) respectively [7, 33].

2.1.1.1 Characteristic drying curve (CDC)

The Characteristic drying curve (CDC) model is a simple lumped model. It uses semi-emperical equations and is computationally inexpensive. It neglects the temperature distribution within particle by considering the Biot number to be small, i.e. that the internal conductive heat transfer resistance is small in comparison to the external convective heat transfer resistance [7].
In the CDC model the drying rate is split into two drying rate regimes. The first drying rate to be described as pure liquid droplet evaporation, often called 'unhindered' or 'constant drying' as the rate limiting step of evaporation is the heat transfer from gas to droplet surface. The constant drying rate is determined at the wet-bulb temperature T_{wb}.
As the droplet dries it will eventually move into the second drying rate regime, described by a 'falling drying' rate. This occurs at the transition from droplet to wet particle stage, where the droplet moisture content surpasses critical content and a shell forms on the surface. The shell impedes the drying rate as it hinders the solvent diffusion from the wet core to the surface, making mass transport the rate limiting step. The falling rate is calculated as a relation between the end drying rate of the first stage and a functional dependence on the characteristic moisture content ϕ. This dependence is adjusted to fit the experimental data of the drying curve.

$$f(\phi) = \frac{N_v}{\hat{N}_v} \tag{2.1}$$

With the constant rate described by an external mass transfer coefficient k_c, vapor pressure above wet surface $P_{v,s}$ and the bulk gas vapor pressure $P_{v,\infty}$,

$$\hat{N}_v = k_c(P_{v,s} - P_{v,\infty}) \tag{2.2}$$

ϕ is described by the current average moisture content X, critical moisture content X_{cr} and equilibrium moisture content X_e. Where both X_{cr} and X_e are experimentally obtained from the sorption isotherm and kept as constant values [34].

$$\phi = \frac{X - X_e}{X_{cr} - X_e} \tag{2.3}$$

f(ϕ) is correlated to the characteristic drying rate curve for the specific material which is retrieved using droplet drying experiments. In the simplest case this correlation could be written as

$$N_v = f(\phi)[k_c(P_{v,s} - P_{v,\infty})] \tag{2.4}$$

By the design of ϕ, f is normalized to move through the critical moisture content point (1,1) and towards equilibrium (0,0), see figure 2.1.

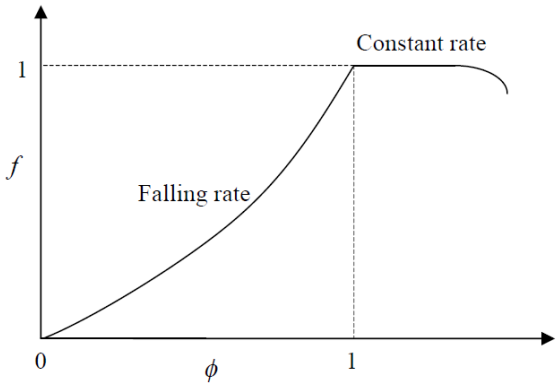

Figure 2.1: Typical characteristic drying curve [7]

Equilibrium is reached when free moisture content X-X_e equals to zero, i.e. when no more moisture is able to leave the solid [30]. Equation 2.4 describing the falling rate is beneficial as it enables study of separate parameters affecting drying, the drying rate of the material f(ϕ), the external conditions affecting mass transfer k_c and the operating conditions described as difference of partial pressure [30].
It should be noted that CDC is based on many idealisations. For example, the mass transfer rate during the unhindered phase is an ideal approximation of the actual rate as the droplet not necessarily has to be at the wet-bulb temperature of the dry gas as the droplet temperature changes during real operation [35]. In addition, for most cases this model assumes the critical moisture content to be constant, which may not be the case. The value of X_{cr} is obtained from the specific droplets studied in the experiment, which size often is many times the usual size of that inside a spray dryer in order to be able to measure the evaporation of mass [7, 24, 30]. Also the critical concentration is affected by the external drying conditions [36]. The

risk is that the experimental setup is inducing errors by affecting the transport of heat and mass or from the discrepancy in scale studied in comparison to the real case. One example of this is the suspended droplet technique where filaments that suspends the droplets may induce a larger heat transfer than in the real case giving erroneous evaporation rates [1, 24].
In summary, CDC can not predict properties of the particle such as temperature distribution or surface composition that would be able to be used indirectly describe the particle morphology. Also it is not possible to tell if part of the particle experience a temperature that exceeds the glass transition temperature and how long period of time this occurs during drying [19].

2.1.1.2 Reaction engineering approach (REA)

REA describes the relative difficulty of evaporating moisture from a droplet as to overcome an activation energy, like a chemical reaction. Similarly to CDC REA is also a lumped model, that doesn't consider the distribution inside the particle. However, REA does not divide the drying rate into two regimes [6, 37].
The initial drying rate of a droplet with a completely wetted surface could be described by a simple rate of mass transfer by convection.

$$m_s \frac{dX}{dt} = -k_c A_{droplet}(P_{v,sat} - P_{v,\infty}) \tag{2.5}$$

Where k_c is taken from a semi-empirical relationship like the Ranz-Marshall. As drying continues the moisture content at the surface eventually decreases leading to a change in surface vapor pressure to $P_{v,s}$, which is time-dependent

$$m_s \frac{dX}{dt} = -k_c A_{droplet}(P_{v,s} - P_{v,\infty}) \tag{2.6}$$

To describe the changing real vapor pressure at the surface to the saturated vapor pressure a fractionality coefficient Ψ is introduced.

$$P_{v,s} = \Psi P_{v,sat}(T_s) \tag{2.7}$$

The values obtained by the fractionality coefficient $\Psi \leq 1$, where $\Psi = 1$ is the completely saturated surface and $\Psi < 1$ when surface enrichment of solutes have begun, "falling rate". Using the idea that relative difficulty of evaporation could be described by overcoming an apparent activation energy, the fractionality coefficient could be described by

$$\Psi = \exp \frac{-\Delta E_v}{RT_s} \tag{2.8}$$

By the lumped approach, i.e. that Bi < 0.1. The temperature distribution is assumed to be uniform, thus setting $T_s = T_d$. Rearranging equation 2.8 and using the definition of Ψ, the activation energy ΔE_v could be described as

$$\Delta E_v = -RT_d log\left(\frac{P_{v,s}}{P_{v,sat}}\right) \tag{2.9}$$

Using equations 2.6 and 2.9 a new equation for ΔE_v can be written as

$$\Delta E_v = -RT_d log\left(\frac{\frac{-dX}{dt} \cdot \frac{m_s}{k_c A_{droplet}} + P_{v,\infty}}{P_{v,sat}}\right) \tag{2.10}$$

Where ΔE_v could be determined from a single accurate experiment run where each experiment setup has the same drying conditions, see figure 2.2.

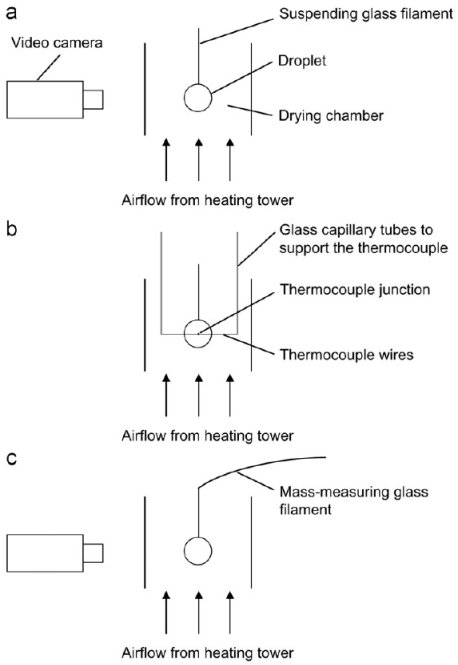

Figure 2.2: Experimental setup, measurement of a) diameter, b) temperature and c) mass, [38].

It is enough to capture rate of mass lost by evaporation, the changing area of droplet and temperature at the droplet surface [39].
Within the REA model materials are empirically correlated to have their specific activation energy curve as a function of their average moisture content relating the difference in vapor pressures at the surface and in the bulk drying gas. The activation energy curve that is retrieved from the specific drying conditions can be normalized with a equilibrium activiation energy to create a master characteristic curve. Where the function $f(X - X_\infty)$ is fitted empirically.

$$f(X - X_\infty) = \frac{\Delta E_v}{\Delta E_{v,\infty}} \tag{2.11}$$

Here $\Delta E_{v,\infty}$ is the maximum activation energy for the same initial size and solid content material under the specific equilibrium moisture content X_∞ when the material reaches the same temperature as the drying air, T_∞. $E_{v,\infty}$ can be retrieved from the sorption isotherm of the material.

$$\Delta E_{v,\infty} = -RT_\infty ln\left(\frac{P_{v,\infty}}{P_{v,sat}}\right) \tag{2.12}$$

To make the model work, it has to be coupled with a general heat balance of the droplet.

$$mCp_d\frac{dT_d}{dt} = hA(T_\infty - T_d) + m_s\Delta H_{vap}\frac{dX}{dt} \tag{2.13}$$

Where mass and heat transfer coefficients are taken from Sh and Nu calculated at initial data with droplet diameter and temperature.
From initial mass and moisture content the apparent activiation energy can be determined from equation 2.11, which can be used to describe the drying rate from the adapted equation 2.6 with the fractionality coefficient. Where the saturation pressure is calculated by initial droplet temperature. The differential equations describing mass and heat transfer are calculated stepwise using a numerical method. Droplet mass, temperature, average moisture content and diameter is updated between each time step.
In summary, the major benefit of REA is that a single master curve can be calibrated and translated to new systems with different drying conditions to describe droplets of other sizes and concentrations. Also the REA is able to predict the diameter during drying, using smooth transition of the drying rates without a critical moisture content criteria [38, 39]. Since the model is lumped it is limited to predicting particle diameter and average moisture content, it can not be used to predict any type of particle morphology. Another issue is the experimental accuracy to reach the empirical correlation between the activation energy of the material and the moisture content [7, 34].

2.1.2 Deterministic models

Deterministic models include mechanistic descriptions of mass and heat transfer for the system as sets of partial differential equations with corresponding initial and boundary conditions. The implementation of this type of model may be more or less troublesome depending on its conceptual basis, eg. if the boundaries move, as the equations still need to be satisfied on the moving boundaries. Furthermore for a purely mechanistic analytical model it is necessary to have total information about the system such as accurate data for every transport phenomena coefficient under each operating condition such as at different temperature or moisture content of either drying gas or particle. The deterministic model is more complex and takes longer time to solve. In addition the problems with the lack of data still needs to be produced either via experiments or by extrapolation of data [33].

2.1.2.1 Shrinking core and wet shell

Shrinking core and wet shell are two models that both utilize the constant drying period, but when the particle shell formation occurs the transport phenomena of the two models are treated differently conceptually.
The shrinking core model assumes a constant particle shell radius in the second drying stage. Also that the shell that is formed is dry and that the solvent and dissolved solid resides into the core, creating a 'wet core'. As drying progresses the solvent is evaporated at the interface of the wet core and the crust, and the interior core receedes inwards. Thus the boundary conditions change with receding

interface. Solvent vapor passes through the porous shell and the solute precipitates at the interior and thickens the shell [7, 14, 34].
In the wet shell model the crust is instead assumed to be flexible (movable), furthermore the solvent diffuses to lie on the outside of the crust (creating a wet shell) and is evaporated. When the particle is heated reaching a temperature high enough the solvent vaporizes within the core generating a bubble, which inflates the particle [7, 17].

2.1.2.2 Diffusion model

Diffusion model, Peclet number analysis or 'VFL' model [1, 13, 23, 40].
The diffusion models considers the mechanism of particle formation using Peclet (Pe) dimensionless number. Pe provides a measure of the relative magnitude of the driving forces of particle formation assuming ideal non-interactive diffusion, no reactions, no surface-active components and absence of internal convection.

$$Pe_i = \frac{\text{Evaporation rate}}{\text{Diffusion}} = \frac{\kappa}{8D_i} \tag{2.14}$$

Here κ is the rate of receding particle area by solvent evaporation whilst D is diffusion coefficient of a component i inside the droplet. Without inclusion of surface-active components, the reduction in volume leads to a concentration gradient which causes components to diffuse inward. The time it takes for the droplet to reach a critical surface concentration and subsequent shell formation can be determined by Pe_i in combination with formulation specific parameters e.g., initial saturation. Pe_i is non-constant as the evaporation rate is dependent on material specific solvent and solute properties and process parameters during drying. A larger evaporation rate, defined by a higher drying gas temperature leads to faster surface enrichment E_i (which is the actual surface concentration of a component in proportion to its average concentration within the droplet)

$$E_i = \frac{C_{s,i}}{C_{m,i}} \tag{2.15}$$

and subsequent shell formation.

2.1.2.3 Maxwell model

The Maxwell diffusion model utilizes a changing Peclet number to describe single droplet drying. Describing the mass transfer of solvent vapor outside the droplet as Ficks first law of diffusion,

$$j = -D\nabla C \tag{2.16}$$

Approximating that the mass flux is independent radially, the equation can solved on the radial coordinate as

$$j = -D\frac{dC}{dr} \tag{2.17}$$

The mass transfer from the sphere is then the mass flux times the total area of the sphere

$$\frac{dm}{dt} = -4\pi r^2 D\frac{dC}{dr} \tag{2.18}$$

With Maxwell quasi-steady state assumptions and boundary conditions the mass transfer and diffusion is independent of the radius, giving

$$\frac{dm}{dt} = -2\pi dD(C_s - C_\infty) \tag{2.19}$$

Where the solvent concentration at the surface is taken from Antoine equation of saturated vapor pressure and the concentration within the gas is taken from the partial solvent pressure in the gas phase.
The change in volume of the droplet is by the mass transfer of solvent, assuming a perfectly spherical droplet gives

$$\frac{dm}{dt} = \frac{d(\frac{\rho\pi d^3}{6})}{dt} \tag{2.20}$$

Considering the density ρ as constant this leads to

$$\frac{dd}{dt} = -\frac{4D(C_s - C_\infty)}{\rho d} \tag{2.21}$$

Which could be regarded as an oversimplification of the system as the density changes with temperature and as temperature changes with time, equation 2.20 is by the chain rule

$$\frac{dm}{dt} = \frac{3\pi\rho d^2}{6}\frac{dd}{dt} + \frac{\rho\pi d^3}{3}\frac{d\rho}{dt} \tag{2.22}$$

Which can be rewritten to form

$$\frac{\mathrm{d}d}{\mathrm{d}t} = \frac{2\dot{m}}{\pi\rho_l d^2} - \frac{d}{3\rho_l}\frac{\mathrm{d}\rho_l}{\mathrm{d}t} \tag{2.23}$$

The heat transfer of the stagnant system is described by conductivity and evaporation. Using analogous Maxwell assumptions the heat balance of the droplet can be described as

$$\rho_l C p_l \frac{d^2}{12}\frac{\mathrm{d}T_d}{\mathrm{d}t} = -k(T_d - T_\infty) - \Delta H_{vap} D_{v,i}(C_s - C_\infty) \tag{2.24}$$

[41, 42]. The internal distribution of solutes within the droplet is assumed to be governed completely by the internal diffusion transport. By assuming constant diffusion, spherical symmetry and moving boundary the one dimensional fickian diffusion with normalized radial coordinate is used, (R=$\frac{r}{r(t)}$).

$$\frac{\partial C_j}{\partial t} = \frac{4D_j}{d^2}\left(\frac{\partial^2 C_j}{\partial R^2} + \frac{2}{R}\frac{\partial C_j}{\partial R}\right) - \frac{\kappa R}{2d^2}\frac{\partial C_j}{\partial R} \tag{2.25}$$

Where the first term on the right hand side is regarded as diffusion, whilst the other term is 'convection', by the innerward movement of the solvent surface from evaporation [40].
With initial condition

$$C_j = C_{j,0}$$

Together with boundary conditions

$$\frac{\partial C_j}{\partial R} = 0, R = 0$$

$$D_j \frac{\partial C_j}{\partial R} - \frac{\kappa}{8} C_j = 0, R = 1$$

Where κ in this model is described as the evaporation rate

$$\kappa = -\frac{dd^2}{dt} \tag{2.26}$$

The second boundary condition is adjusted from [43] when no solute is assumed to move into the gas. Which states that the diffusion and convective flux are equal at the liquid-gas interface.

2.1.2.4 VFL model

An analytical solution (VFL model) was derived from diffusion models by [23], to describe the radial distributions of components within droplet assuming constant evaporation rate. In order to have analytical solutions the components are assumed to exhibit ideal non-diffusion interaction, constant diffusion along with no internal convection.
The constant evaporation rate is described by the d^2 law,

$$d^2(t) = d_0^2 - \kappa t \tag{2.27}$$

where d_0 is the initial droplet diameter, and κ the receding surface rate. It assumes that the evaporation occurs solely at the wet bulb temperature.
From the assumptions the radial distribution of solute concentrations can be described by Ficks second law

$$\frac{\partial C}{\partial t} = D \frac{\partial^2 C}{\partial z^2} \tag{2.28}$$

The solution of Ficks second law in normalized radial coordinate system leads to a relationship between concentration of solute i C_i in the radial and time coordinates the mean concentration $C_{m,i}$ at time t and the Peclet number of solute i.

$$C_i(r,t) = C_{m,i}(t) \frac{exp\left(\frac{1}{2} Pe_i R^2\right)}{3 \int_0^1 R^2 exp\left(\frac{1}{2} Pe_i R^2\right) dR} \tag{2.29}$$

For a constant drying rate κ and constant diffusion coefficients, the Pe is constant for every solute i.
Assuming that no solute is lost to the ambient as the droplet dries a conservation mass balance can be used to calculate the mean concentration of solute i inside the droplet as,

$$C_{0,i} \cdot \frac{\pi d_0^3}{6} = C_{m,i}(t) \cdot \frac{\pi d(t)^3}{6} \tag{2.30}$$

Using the approximate drying time from equation 1.10 and constant evaporation rate from equation 2.27, equation 2.30 is simplified to

$$C_{m,i}(t) = C_{0,i}\left(1 - \frac{t}{\tau_D}\right)^{\frac{-3}{2}} \tag{2.31}$$

With this analytical model there are several characteristic times that can be applied to follow general trends to predict the droplet drying evolution and the components radial distribution prior to solidification of the particle, if the evaporation rate is accurate. Some of these are characteristic time to reach saturation at the surface $\tau_{sat,i}$, when the concentration of solute i becomes the same as the initial saturation. The precipitation window $\tau_{p,i} = \tau_D - \tau_{sat,i}$, and the time it takes for surface concentration to reach particle true density (time when shell forms) $\tau_{t,i}$.
From the d^2 law in equation 1.10 describing the maximum drying time and the definition of Peclet in equation 2.14, the VFL states a simplified equation describing the surface enrichment E of a component i as

$$E_i = \frac{C_{s,i}}{C_{m,i}} = 1 + \frac{Pe_i}{5} + \frac{Pe_i^2}{100} - \frac{Pe_i^3}{4000} \tag{2.32}$$

Where again, the $C_{m,i}$ is the average concentration. With the initial saturation of the component written as

$$S_{0,i} = \frac{C_{0,i}}{C_{sol,i}} \tag{2.33}$$

the time to reach saturation at the surface (reach critical concentration) is in the VFL model approximated as

$$\tau_{sat,i} = \tau_D\left(1 - (S_{0,i}E_i)^{\frac{2}{3}})\right) \tag{2.34}$$

To summarize, the analytical VFL model fails to capture non-stationary operating conditions when temperatures are changing. Such as the beginning with droplet sensible heating and end of drying, with shell formation and droplet temperature increase. Furthermore, diffusion coefficients of solutes and excipients are not constant during real drying. They change with the change in concentration, temperature and mobility. Therefore the model can not predict diffusion by mobility issues such as precipitation by supersaturation or elevated viscosity before shell formation. In addition it can not directly for-tell solidification or morphological change [1, 13, 22, 23].

2.1.3 Review of models

From the literuture review it is clear that particle engineering models are made to either make fast outlet predictions for spray drying operations such as average moisture content and particle size conditioned on the absence of morpohological development like buckling or inflation (CDC,REA) [6, 30, 37, 39]. With diffusion models (Maxwell, VFL) it is possible to examine the distribution of solutes within

droplet/particle during drying to predict onset of shell formation and make 'indirect' prediction of morphology [1, 13, 23]. Other articles soughts to enhance CFD simulations with simple droplet drying models describing heat and mass transport, enabling simulations of eg. sticky particle deposition by describing average temperature and moisture content (CDC,REA) [5, 30].

2.2 Models for Particle Morphology Prediction

Neither CDC nor REA does directly describe morphology as they are lumped models. However, they can be used to predict diameter and density. Use of semiempirical correlations with these models can indirectly describe morphological events such as buckling. The critical parameters retrieved from experiments used for deriving the models are perhaps the ones that are most indicative, such as the critical moisture content before shell formation [37]. The main feature of the semiempirical models is how the drying kinetics is conceptualized in the second drying stage. Figure 2.3 reflect on possible morphology mechanisms in the second stage of drying.

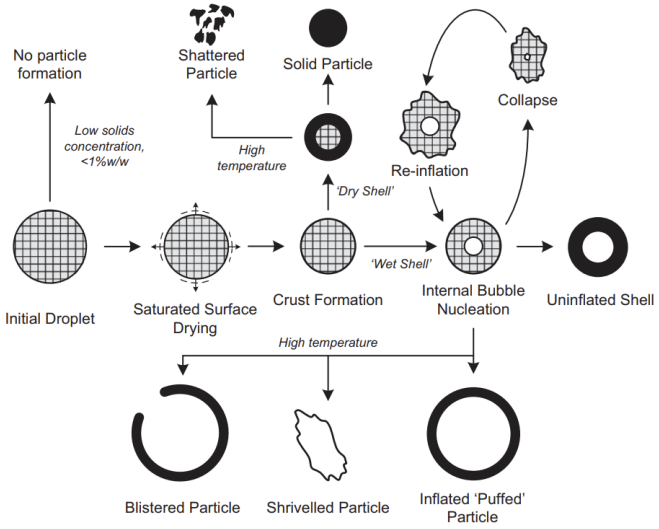

Figure 2.3: Schematic of different particle morphologies, [44].

The shrinking core model is able to predict solid particle formation, whilst the wet shell model is a feasable option to describe hollow, shriveled or puffed particles [17, 44].
The diffusion model has two solutions. One of them assume a constant Pe (analytical) calculated prior drying, the other use a Pe that is changing during drying. Depending on the variant of the solution it is possible to attain different levels of detail. A changing Pe is by default better at predicting the spatial distribution of the solutes. The analytical solution with Peclet number analysis is able to indirectly capture some qualitative morphological properties of particles. The analysis can be divided into two regions, Pe<1 and Pe>1. Generally these values are able to predict high or low density particles respectively. When Pe is low (Pe<1) the evaporation rate is slow and the solutes have sufficient time to diffuse inwards, leading to low

surface enrichment until a small highly dense particle is formed. A Pe which is large (Pe>1) quickly leads to high surface enrichment as diffusion inwards of solute is much slower than the receding surface from evaporation, creating larger mostly hollow particles. Depending on the structural integrity decided by the thickness and rigidity of the skin and the external forces it experience during drying the particle can stay spherical or collapse and shrivel [23]. In figure 2.4 the qualitative influence of Pe number on the shell formation and final particle morphology is shown.

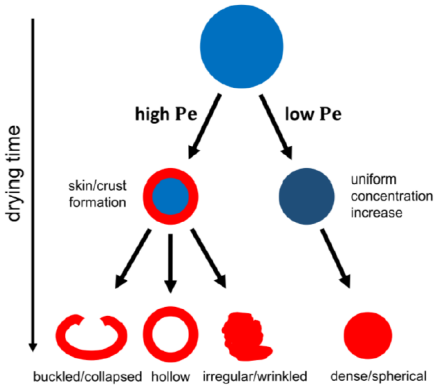

Figure 2.4: Schematic illustration of the influence of the drying conditions and formulation properties/composition (represented in PE) on the final morphology, [11].

The changing Pe solution to the diffusion model is able to predict droplet drying progression in terms of droplet size by radius, mass, density, remaining solvent along with radial distribution profiles of solutes in the space and time domain. With predetermined data of supersaturation of the solute it is possible to predict onset of shell formation at the droplet surface. For systems where particle formation is triggered by phase separation, the mechanisms onset can also be used to predict final particle properties such as size and density. (A Pe>1 forms less dense wrinkled or hollow particles, whilst Pe<1 leads to dense particles) [13].
The drawbacks with this model is e.g. the drying rate from d^2 law, with constant time-, concentration and temperature independent internal diffusion coefficient. The constant Pe solution (constant diffusion coefficient) is blind to the particle formation mechanism. As particle formation commences, the mobility of solutes are no longer determined by diffusion, but by the solidification pathway of solute(s) which reach their critical concentration. At this point Pe should rapidly increase. Depending on remaining drying time, solubility limit and the propensity of crystallisation the solutes can either precipitate or form a highly viscous shell, a glass. The solutes which precipitate create phase separated domains at the droplet surface, hindering the mobility of other solutes to reach the surface [1, 13, 22].

2.3 gPROMS Model validation

A model or process is built using a mathematical description of the chemo-physical phenomena occurring within the system boundaries. Transport phenomena coeffi-

cients or parameters used can be altered to enhance the predictability of the model, i.e. how well the model describes the real system. Model validation is a statistical analysis method of working with experimental data created from performed experiments and chosen measurements to fit or to approximate values of model parameters which are unknown.
In gPROMS the Maximum likelihood (ML) method is used to estimate both parameters inside system- and variance model that describes the accuracy of experimental measurement. ML uses an objective function, a 'likelihood function' $\mathrm{L}(\theta|X_1,..X_n)$, which aims to find the most likely value of the unknown parameters θ given the data observed X. The likelihood function searches for the value of θ which maximize the statistical probability of the model to predict reality, the experimental data. This value of θ is called the maximum likelihood estimator (MLE). When the variance model is assumed to exhibit constant variance, (eg. $\pm$ 1K for temperature measurements) the ML only searches for values of model parameters.
Assuming that X is a random variable (in this case fixed experimental observation) which is also independent and identically distributed drawn from a probability distribution $\eta(X_i, \mu, \sigma^2)$. The joint probability distribution of a sample of random variables with the only unknown as the parameter θ is equal to the likelihood function.

$$L(\theta|X_1,..X_n) = \eta(X_1, \mu, \sigma^2) \cdot ... \cdot \eta(X_n, \mu, \sigma^2)$$

In essence the idea of the maximum likelihood estimator (MLE) is to find parameter values maximizing L, thus the idea to choose (μ, σ^2) that maximizes

$$\hat{\mu}, \hat{\sigma}^2 = \max_{\mu,\sigma^2} \Pi_{i=1}^{N} \eta(X_i, \mu, \sigma^2)$$

[45, 46].
To quantify how well the parameter estimation was able to predict the actual values the root mean square error (RMSE) was calculated. RMSE estimates the standard deviation σ of the distribution of residuals, the errors.

$$\mathrm{RMSE} = \sqrt{\Sigma_{i=1}^{n} \frac{(y_i - \hat{y_i})^2}{n}} \tag{2.35}$$

Where the observed experimental values are y_i, the predicted values $\hat{y_i}$ and n is the number of observations within the population. The empirical rule of statistics tells that for observations following a normal distribution 95 % fall within two standard deviations. It should however be noted that by the squaring within the calculation of RMSE outliers get a disproportionate impact.

3
Method

3.1 Problem definition

A model describing spray drying within the drying chamber was created by coupling single droplet drying model with size distribution calculations and a thermodynamic dryer model. The model was used to evaluate the influence of some critical parameters such as critical concentration and diffusion coefficient on particle formation.
Available data in-house prove that specific surface area (SSA) do not change significantly after shell formation. Thereby SSA is capable to act as a measurement variable in gPROMS model validation to capture critical parameters of shell formation by fitting SSA from simulation to experimental data. The critical parameters derived were regarded as scale independent and tested for transfer across spray drying scales and formulations. Heat losses of the spray dryer were also derived from parameter estimation of experimental data.
Experimental data of spray drying was used from three different spray dryers, the labscale Buchi Mini Spray Dryer B-290, Anhydro Micraspray MS35 and AstraZeneca (AZ) spray dryer. The spray drying formulations in experiments had water as solvent with different combinations of solute components; API, buffer and excipients that are named A, B, and C through the report.

3.1.1 Shell formation implementation in model

In this model the main focus was capturing the droplet to particle transition, the onset of shell formation. Shell formation is implemented in the model as the critical concentration of the respective components within the formulation. For shell formation to occur it is only necessary that one of the components reach their critical concentration.

3.1.2 Model setup in gPROMS

Within gPROMS the model is defined as a hierarchical composite model where the higher level model calls upon instances of lower level models. The model instances transfer inputs and outputs at each simulation step by connecting equations within the higher level model. In that way the troubleshooting is simplified drastically [46, 47]. Built on this structure, 4(5) model components were defined and constructed for single droplet drying. The 4 submodels are named 'Energy', which calculate the energy balance over the droplet, 'Mass' component evaluating the leftover solvent

mass, 'Size' for diameter prediction and lastly a 'Internal radial distribution' component for the internal radial distribution of solutes. The higher level model (5) calling on the submodels is the Drying model. In figure 3.1 the relationship of the sublevel models to the higher level model is depicted.

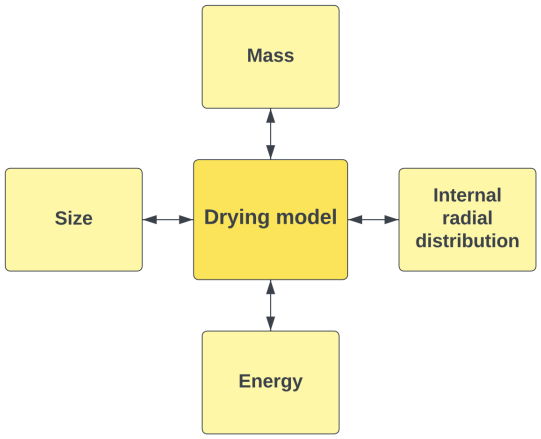

Figure 3.1: Drying model component layout

All sublevel models are solved simultaneously within gPROMS.

3.1.3 Model assumptions

1. Drying and atomizer gas follows the ideal gas law.
2. No heat is transferred via radiation.
3. The droplets/particles are spherical.
4. Droplets/particle experience no internal circulation, rotation or shape oscillation.
5. The droplets/particles are spread homogenously over the domain, with no interactions either to other droplets/particles or the walls.
6. 'still gas approach' - the relative velocity between the droplet/particle to the atomizer and drying gas is zero.
7. The droplet surface is instantaneously surrounded by a saturated vapour film when introduced to the drying chamber.
8. The droplet temperature is uniform.
9. No reactions.
10. Transport of solvent within the droplet/particle is unrestricted and occurs instantaneously.

3.2 Drying model

This section gives the formal drying model proposal with all components implemented. The gPROMS code can be seen as a whole in the appendix A.6.

3.2.1 External heat and mass transfer estimation

3.2.1.1 'Still gas'

For the single droplet drying model the 'still gas' approximation is used, i.e. that the droplets are moving with the same velocity (stagnant droplets/particles). "Still gas" approximation can be motivated by that the droplet/particle always resides in the drying gas flow, with the time the relative velocity difference the droplet experiences from the nozzle to the final settling time within the spray dryer body is low in comparison to the total chamber residence time [4, 9, 41]. In addition with the zero relative velocity, the shear stress acting on the liquid-gas interface becomes zero and will not induce any internal convective circulation [48]. With the 'still gas' approximation the only mode of heat and mass transport in between the droplet/particle and drying gas is through conduction and diffusion respectively.

3.2.1.2 Evaluation of heat transport

Based upon the 'still gas' approximation the choice of using lumped or uniform temperature distribution within the droplet can be justified by evaluating the internal and external heat transport resistances using the dimensionless Biot number, (Bi). Biot number is defined as the ratio between the resistance for conduction within the body to the resistance from convection at the surface of the body.

$$Bi = \frac{Nu \cdot k_{ext}}{k} = \frac{h_{ext} L}{k} \tag{3.1}$$

Where h_{ext} is the external convection, L as the characteristic length of the system and k as the internal conduction of the droplet.
A Biot number that is less than 0.1 indicate that the temperature inside the spatial domain of the body not vary significantly, in other words the heat transport is externally controlled and a lumped approach could be employed. Whereas a $Bi > 0.1$ entails the opposite with an internal controlled process where it is necessary to describe the internal domain as distributed. The error with using a lumped compared to distribution approach is typically less than 5% [49].
With no relative velocity, the external convective heat transfer coefficient can be derived from a Nusselt correlation of natural convection.

$$Nu_D = 2 + 0.43 Ra_D^{1/4} \tag{3.2}$$

Where Ra_D is the Rayleigh number describing the relative time scales of thermal transport via diffusion and convection. Ra_D is the product of the Grashof (Gr) and Prantdl (Pr) dimensionless numbers [49]. Evaluating these numbers within the temperature domain and with the maximum initial size of droplet taken from typical drying conditions of inhalation powders Ra_D approaches zero. This means that heat transfer from the surrounding drying gas to the surface of the droplet/particle is occurring with conduction, with the upper limiting value Nu_D of 2.
Evaluating Bi at process conditions, approximate values of $k_{N_2} = 0.03$ W/mK, with water heat conductivity k = 0.6 W/mK, yields Bi = 0.1 which makes the lumped approach applicable.

3.2.1.3 Evaluation of mass transport

Similarly the mass Biot dimensionless number was used to evaluate the internal and external mass transport resistances. The mass Biot number is completely analogous to the heat Biot number.

$$Bi_m = \frac{h_{m,ext}L}{D} \tag{3.3}$$

Where $h_{m,ext}$ is the external mass transport by convection and D is the internal diffusion mass transport. Considering a droplet with solutes and solvent which is unbounded in terms of internal transport the solutes would be evenly spread throughout the droplet, and their concentrations at any point in time could be calculated from a mass conservation balance. However, as reported by Van Der Lijn [50], the mass transport inside the droplet is bound by internal diffusion, meaning that the solutes are to be accounted as distributed inside the droplet with corresponding concentration gradients.
Evaluating Bi_m from the process conditions when using the zero relative velocity assumption, the Sherwood number (Sh) from Ranz-Marshall correlation is 2. Using the definition of Sh,

$$Sh = \frac{h_{m,ext}L}{D_{AB}} \tag{3.4}$$

and approximating the binary mass diffusivity of water vapor in nitrogen gas as water vapor in air at 298 K and atmospheric pressure, $D_{AB}P$ (m^2Pa/s) = 2.634. The internal diffusion D is approximated as constant diffusion of a solute, $5{\cdot}10^{-10}$ m^2/s taken from literature [23]. Putting all approximations together give $Bi_m \approx 1 \cdot 10^5$. Thus, the mass transfer must be solved in the internal spatial domain of the droplet.

3.2.2 Model components

3.2.2.1 Energy

The droplet energy balance consists of heat accumulation, energy flux to and from the system and heat lost due to solvent evaporation. Since the energy transfer occurs at near ambient conditions the heat transfer from radiation is assumed to be negligible. Also assuming that the relative velocity between the gas and the droplet/particle is zero, i.e. 'still gas', there is no convectional heat transfer. The heat flux is then only described by conduction. From Fouriers law the heat flux is written as

$$q = -k\frac{dT}{dr} \tag{3.5}$$

which could extended into the energy transfer to the spherical surface as

$$Q = -4\pi r^2 k\frac{dT}{dr}. \tag{3.6}$$

Using the quasi-steady state assumption makes Q independent of the radius, as derived from Finlay [42], its possible to integrate from the droplet/particle surface to the bulk, which gives

$$Q = -2\pi dk(T_s - T_\infty). \tag{3.7}$$

The evaporative heat transferred away from the droplet/particle is described as

$$E = \Delta H_{vap} \frac{dm}{dt} \tag{3.8}$$

Using equations 3.7 and 3.8 with the ackumulation term the total droplet/particle energy balance is written as

$$mCp_l \frac{dT_d}{dt} = -2\pi dk(T_d - T_{gas}) + \Delta H_{vap} \frac{dm}{dt} \tag{3.9}$$

To follow the physical phenomena of drying the droplet should first heat up from the initial inlet temperature of the solvent to the wet bulb temperature, as described by constant drying. To check that the conditions match, it is possible to use a Mollier diagram with absolute humidity Y and the gas temperature T_{gas} to quickly retrieve an approximate T_{wb}. As an example a dryer with Y = 0.007, T_{gas} = 69°C would give a $T_{wet,bulb} \approx$ 30°C from viewing the diagram.
The transition to the second stage occurs as the critical concentration is reached. In this model the droplet/particle temperature change is not formulated beyond transition and is just described as a discrete step, stating

$$T_d = T_{gas} \tag{3.10}$$

3.2.2.2 Mass

The evaporative mass transport via diffusion is taken as derived in section 2.1.2.3.

$$\frac{dm}{dt} = -2\pi dD(C_s - C_\infty) \tag{3.11}$$

The initial condition to equation 3.11 is the intial solvent mass, calculated as

$$m_{initial} = \frac{\rho \pi d_{initial}^3}{6}. \tag{3.12}$$

To determine the drying rate of solvent it is enough to combine the transport occuring outside the droplet with the equilibrium solvent vapor pressure [50]. Assuming a quasi-steady state the surface concentration is calculated assuming equilibrium instantaneously sets in at each time step,

$$P_{sat,surface} = f(T_d), \text{at r} = \frac{d}{2}, \forall t > 0. \tag{3.13}$$

In addition assuming that the equilibrium vapor pressure is dictated solely by the temperature within the droplet (instead of the concentration of the solvent on the surface of the droplet), the Antoine equation describing the saturated vapor pressure at the surface was used

$$log_{10}(P_{sat,surface}) = A - \frac{B}{T_{droplet} + C} \tag{3.14}$$

The surface concentration C_s is taken from the ideal gas law as

$$C_s = \frac{P_{sat,surface} M_{H_2O}}{RT_d} \tag{3.15}$$

At the second stage, the drying stops.

$$\frac{dm}{dt} = 0 \tag{3.16}$$

In reality droplet drying still continues through the shell, but is dependent on the shell permeability of solvent vapor diffusion [14].

3.2.2.3 Size

As droplets have low loading of solids, i.e. dilute system it is applicable to use constant density. (Using the equation 2.23 with a changing density led to a high index problem). Using the theory of section 2.1.2.3, gives

$$\frac{dd}{dt} = -\frac{4D(C_s - C_\infty)}{\rho d} \tag{3.17}$$

The initial droplet size is calculated from droplet size distribution, which is dependent on the number of different droplet sizes, i.e. the number of bins utilized.
In the second stage, the droplet is assumed to not shrink any further.

$$\frac{dd}{dt} = 0 \tag{3.18}$$

3.2.2.4 Internal Radial distribution of solutes

The internal distribution of solutes is calculated using theory of section 2.1.2.3, giving

$$\frac{\partial C_j}{\partial t} = \frac{4D_j}{d^2}\left(\frac{\partial^2 C_j}{\partial R^2} + \frac{2}{R}\frac{\partial C_j}{\partial R}\right) - \frac{\kappa R}{2d^2}\frac{\partial C_j}{\partial R} \tag{3.19}$$

with the same initial and boundary conditions. The evaporative rate κ is taken from equation 2.26.
It is assumed that the radial distribution of components solely is affected by their respective diffusion coefficients. Surface-active behaviour of components is not accounted for. The model was formulated to be able to describe the component diffusion either as constant value found from literature or via the Stokes Einstein equation,

$$D_{AB} = \frac{k_B T}{6\pi\mu_w R_A}. \tag{3.20}$$

Where D_{AB} is the diffusion in m^2/s, stefan-boltzmann constant $k_B = 1.38 \cdot 10^{-23}$ kgm^2/s^2K, μ_w is the solvent viscosity in Pas and R_A is the molecular radius of the solute in m.

Within the Stokes-Einstein diffusion equation it is possible to describe the diffusion of a solute in a solvent where the effects of pure solvent viscosity is included.
An important remark from literature is that several studies reflect on the effects of changing viscosity on solute mobility [1, 22, 23]. At high solid concentrations the mobility of components are affected by the increasing viscosity. To reduce the risk of phase separation and create a stable drug, the viscosity should increase quickly to 10^{12} - 10^{14} Pas [8]. However, as a simplification this has not been taken into account.

3.3 Overall model

In order to simulate the entire spray drying operation, the model was extended to simulate simultaneous drying of multiple droplet sizes from a size distribution. Also, the specific spray dryer setting was added via a spray dryer thermodynamic model. To couple the drying model with the droplet size distribution and the thermodynamic spray dryer model 3(4) model components were used. In figure 3.2 is the layout of the overall model, it show the relations between the 'Drying model', 'Atomization model' to calculate the droplet size distribution and 'Spray dryer thermodynamic model' as submodels to the higher level model, the 'Overall model'.

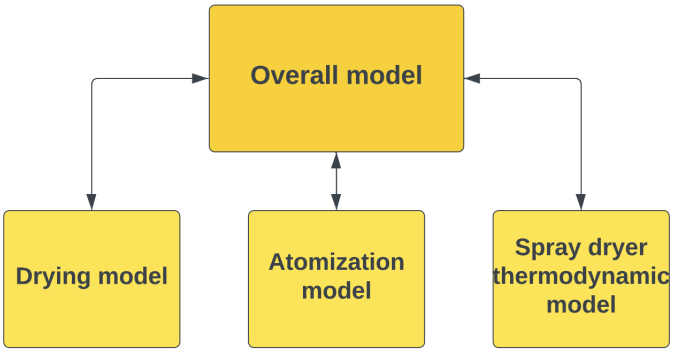

Figure 3.2: Overall model layout

3.3.1 Atomization model

A single droplet drying model can be extended to work for the whole size range of droplets generated from the atomizer. By coupling the internal and external heat and mass transport of each droplet with the dryer model the single droplet drying within the chamber is described. Discretizing the droplet size distribution from the atomizer into bins, the drying of all the droplets within the spray dryer can be calculated. Three quantiles, d10, d50 and d90 of the droplet size distribution had in earlier works been calculated by fitted regression to the specific atomizer nozzle of each spray dryer setup. The extended Swanson-Megill method [51] was used to calculate an estimate of the normal distribution mean $\hat{\mu}$ and variance $\hat{\sigma}^2$ from the three quantiles,

$$\hat{\mu_n} = 0.4d_{50} + 0.3(d_{10} + d_{90}) \tag{3.21}$$

$$\hat{\sigma_n}^2 = 0.4(d_{50} - \hat{\mu})^2 + 0.3[(d_{10} - \hat{\mu})^2 + (d_{90} - \hat{\mu})^2] \tag{3.22}$$

Assuming that the droplets are distributed like a log normal distribution, the mean μ_n and the variance σ_n from the normal distribution can be used to calculated the log normal mean μ and variance σ [52] as

$$\mu = log_e\left(\frac{{\mu_n}^2}{\sqrt{{\sigma_n}^2 + {\mu_n}^2}}\right) \tag{3.23}$$

$$\sigma = \sqrt{log_e\left(1 + \frac{{\sigma_n}^2}{{\mu_n}^2}\right)}. \tag{3.24}$$

The cumulative lognormal distribution function is described as

$$\text{CDF}(d) = \frac{1}{2}\text{erfc}\left(\frac{\mu - log(d)}{\sqrt{2}\sigma}\right), d > 0 \tag{3.25}$$

Using the definition of erfc,

$$\text{erfc}(z) = 1 - \text{erf}(z) \tag{3.26}$$

with

$$\text{erf}(z) = \frac{2}{\sqrt{\pi}}\int_0^z e^{-t^2}dt \tag{3.27}$$

Leading to the final expression for the equation 3.25 as

$$CDF(d) = \frac{1}{2}(1 - \frac{2}{\sqrt{\pi}}\int_0^{\frac{\mu - log(d)}{\sqrt{2}\sigma}} e^{-t^2}dt) \tag{3.28}$$

The volume fraction that the diameter ranges d_i to d_{i+1} occupy is calculated as

$$V_{frac} = CDF(d_{i+1}) - CDF(d_i) \tag{3.29}$$

The total volume of the droplets at the edge of the nozzle can be calculated as

$$\dot{V} = \frac{\dot{m}_{feed}}{\rho} \tag{3.30}$$

The amount of droplets in the diameter ranges d_i to d_{i+1} is then evalauated as

$$\theta_{d_{i+1}-d_i} = \frac{\dot{V} \cdot V_{frac}}{\frac{\pi}{6}\left(\frac{1}{2}(d_{i+1} + d_i)\right)^3} \tag{3.31}$$

The droplets within the range is then assumed to be of the same size, i.e the average diameter of the upper and lower bound.

$$d_{mean} = \frac{1}{2}(d_{i+1} + d_i) \tag{3.32}$$

In gPROMS it was not possible to solve the CDF directly, as the results of CDF either gave numbers larger than 1 or a oscillatory solution when the diameter was increasing, see figure 3.3.

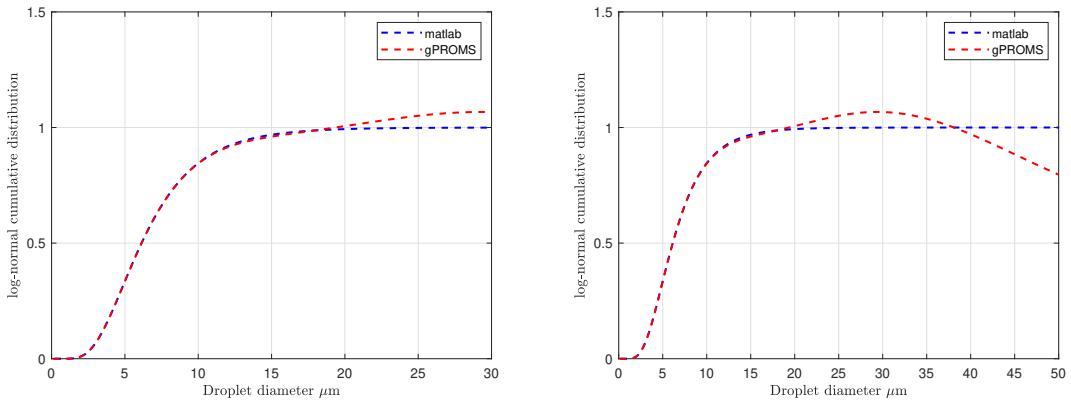

(a) to 30 μm diameter **(b)** to 50 μm diameter

Figure 3.3: Example of CDF calculations, comparing matlab and gPROMS performance

By definition the value of CDF could not exceed 1, nor could it change shape as it is a strictly positive monotonic function. The calculation was also checked and performed with matlab, which gave good results. However, the implementation of importing matlab data into gPROMS turned out to be cumbersome and with low flexibility for introduction of new experimental data. As a band-aid solution in gPROMS, the generated CDF values were all normalized with the CDF corresponding to the largest droplet, to give CDF values in between 0 and 1.

The lognormal cumulative distribution of all the dryers are shown in figure 3.4. The CDF, volume fractions and number of droplets per droplet diameter θ, for each dryer is taken from each respective most common experiment process conditions.

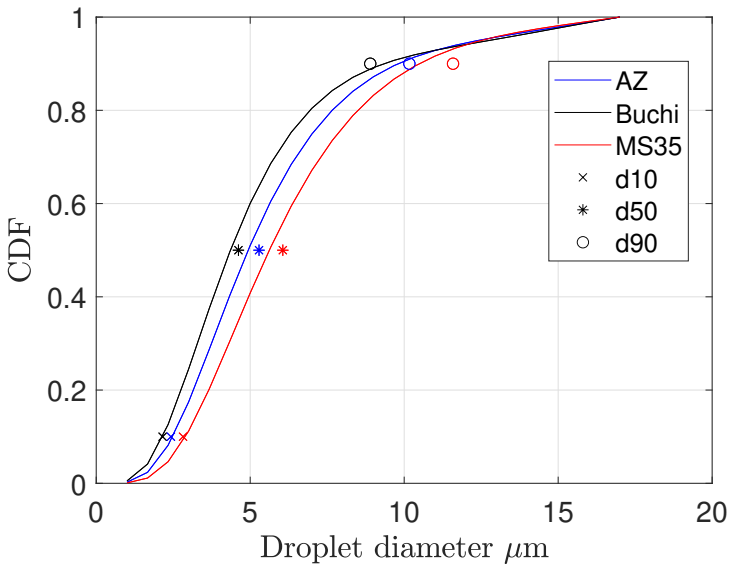

Figure 3.4: CDF for all the spray dryers

The figure shows qualitatively that the calculated CDF from theory follow the quantiles d10, d50, d90 calculated from the regression equation, marked with 'x', '*', 'o' quite well. Quantitively, the average of each quantiles relative error (with the regression quantiles as reference) is used to describe how well the quantiles from the distribution correlate to the ones from the regression.

Table 3.1: Relative error quantiles in %

Dryer type	d10	d50	d90
AZ	1.6	-6.7	-4
Buchi	-1.2	-5.6	5.2
MS35	2.4	-7.3	-10

The figures 3.5, 3.6 and 3.7 below show the number of droplets per droplet diameter and volume fractions of each dryer at the start of drying.

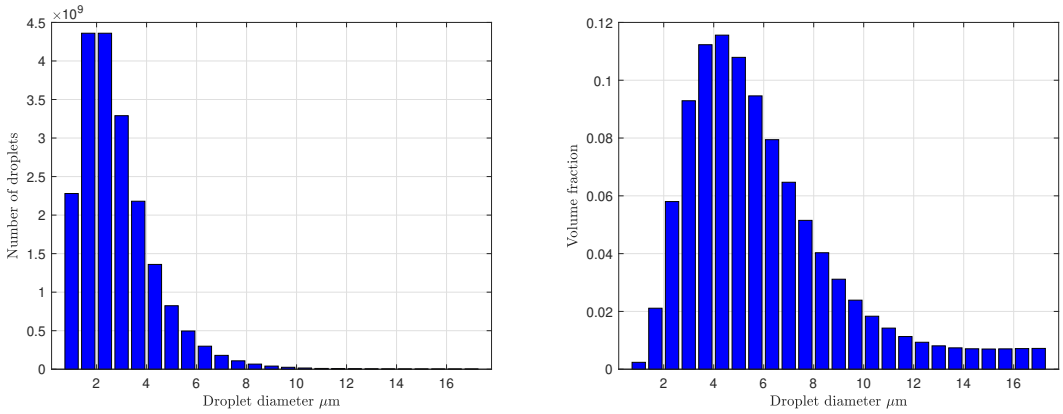

(a) θ, number of droplets per droplet size**(b)** Volume fraction per droplet size

Figure 3.5: AZ dryer atomization model results

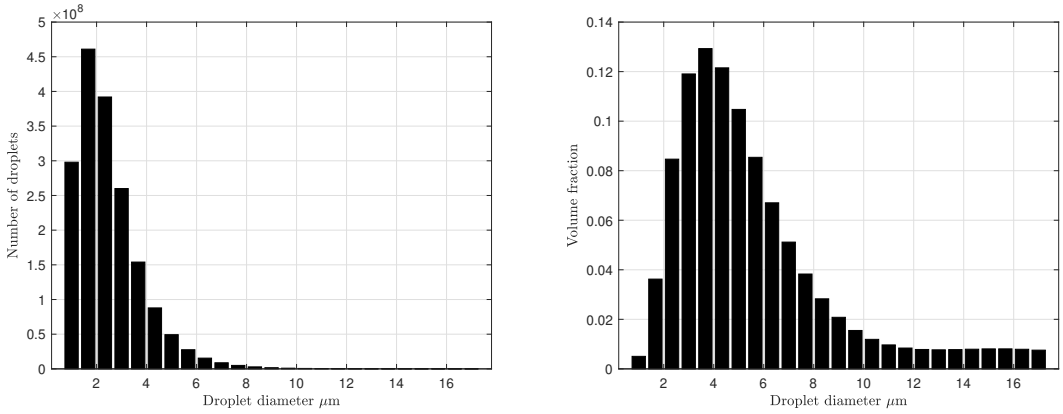

(a) θ, number of droplets per droplet size**(b)** Volume fraction per droplet size

Figure 3.6: Buchi atomization model results

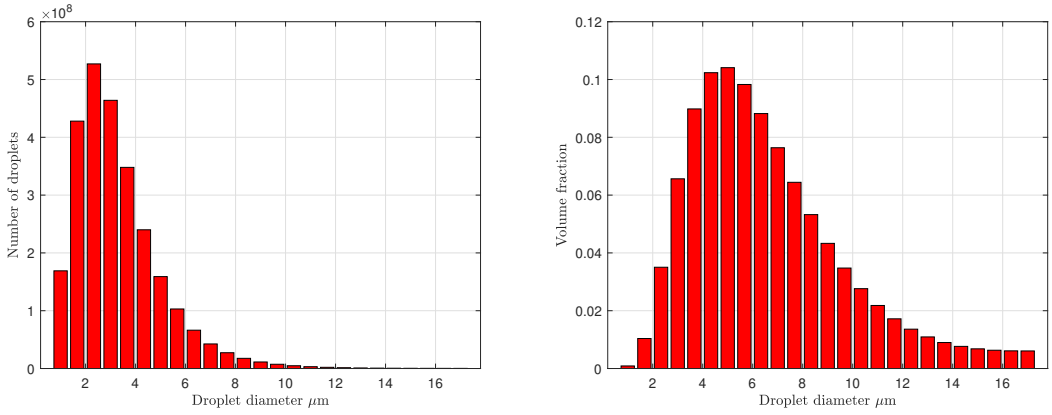

(a) θ, number of droplets per droplet size**(b)** Volume fraction per droplet size

Figure 3.7: MS35 atomization model results

3.3.2 Spray dryer thermodynamic model

Two different models, the continously stirred tank reactor (CSTR) and the plug flow reactor (PFR) were reviewed.

For final model implementation CSTR model was chosen as the dryer model, as it would be simple to implement and also that it correlate reasonably well with the overall drying temperature the droplet would experience during its lifetime. Describing the residence time of the droplet within the spray dryer was not taken into consideration as the interest lied solely in when the droplet would transition into the particle state.

The CSTR flow model assumes a perfectly mixed situation, where the injected droplets are instantaneously subjected to the outlet drying conditions. The outlet conditions are assumed to be constant and are calculated directly from macroscopic heat and mass balances.

The application of CSTR as the dryer model is motivated by its inherent simplicity and is supported by CFD results found in literature showing the temperature evolution within the spray dryer body [25] aswell as the overall residence time of the droplet/particle inside the spray dryer body, where a relatively short time is spent close to the atomizer [4, 15].

At steady state, a macroscopic heat balance can be used to calculate gas outlet temperature. See equation A.19. The drying gas inlet temperature is measured at a distance from the actual inlet of the drying chamber, thus a heat loss constant h_{pipe} (W/K) is used to estimate the heat loss that drying gas experience at the inlet pipe prior to the drying vessel. This value is derived from parameter estimation using experimental results.

From a macroscopic mass balance, the absolute humidity is estimated assuming that all incoming moisture within the feed is evaporated.

$$Y = \frac{\dot{m}_{feed}}{\dot{m}_{ag} + \dot{m}_{dg}} \tag{3.33}$$

The concentration of solvent in the gas is calculated from the relationship between the saturation pressure at gas temperature, the absolute and relative humidity and the ideal gas law.

$$log_{10}(P_{w,sat}) = 10.113 - \frac{1685.6}{T_{gas} - 43.154} \tag{3.34}$$

From earlier the relative humidity could be written as

$$\phi = \frac{P_{tot}Y}{(\frac{M_w}{M_{N_2}} + Y)P_{w,sat}}. \tag{3.35}$$

The solvent concentration within the gas could then be calculated as

$$C_{w,\infty} = \frac{P_{w,sat}\phi M_i}{RT_{gas}}. \tag{3.36}$$

3.4 Considering heat losses from dryer

For all the spray drying experiments the inlet and outlet temperature of the drying gas is measured. What changes with the different dryer setups is where these thermocouples are placed. If the inlet temperature is taken within the pipe leading to the spray drying vessel which is located a bit upstream from the actual inlet heat loss from the pipe to the surroundings should be accounted for. For all spray dryers heat loss is occurring from the spray dryer body. Heat loss is evaluated as the loss by convective heat transfer from the drying gas inlet pipe and from the body. Heat losses from conduction and radiation is neglected. Only steady state heat losses are considered, as the accumulation of energy in the pipe material is assumed to be negligible.
Without solids interfering with drying the equations describing the heat transfer rate using Hess law can be described as

$$\begin{aligned} \dot{m}_{dg}Cp_{dg}T_{in,dg} + \dot{m}_{ag}Cp_{ag}T_{in,ag} = \dot{m}_{dg}Cp_{dg}T_{out} + \dot{m}_{ag}Cp_{ag}T_{out} \\ + \dot{m}_{feed}\Big\{ Cp_{water,liq}(T_{evap} - T_{feed,in}) \\ + \Delta H_{vap} + Cp_{water,vap}(T_{out} - T_{evap}) \Big\} \\ + \text{Heat loss} \end{aligned} \tag{3.37}$$

The left hand side of equation 3.37 accounts for the incoming heat to the vessel by the drying and atomizer gas. Whereas the right hand side accounts for the phase change, evaporative heat, the outgoing heat from the vessel and the heat loss. The total heat lost is described as the heat lost from both the pipe and the body.

$$\text{Heat loss} = h_{pipe}(T_{in} - T_{amb}) + h_{body}(T_{out} - T_{amb}) \tag{3.38}$$

Where the loss in the pipe is assumed to be dependent on the $T_{dg,in}$ and the loss in the body on T_{out}. The reason for this approximation is that in a typical spray dryer the temperature inside the dryer develops to the outlet temperature close to the atomizer, as seen from the CFD results [25] in figure 1.11.
Utilizing Hess law the values of the properties are taken at 25°C, and presented in table 3.2

Table 3.2: Material properties

ΔH_{vap} (kJ/kg)	Cp_{N_2} (J/kgK)	$Cp_{w,liq}$ (J/kgK)	$Cp_{w,gas}$ (J/kgK)
2441.7	1040	4184	1864

3.5 Critical properties of spray dried powders

3.5.1 Particle size

To check the validity of the literature values of the critical concentrations and constant diffusion, the dry particle $d_{p,50}$ was seen as a possible measurement variable in

the parameter estimation. Final experimental results of dry particle d_{10}, d_{50} and d_{90} were available. In order to use these results, one had to assume that the distribution of the particles collected after the cyclone was the same as the end of the spray dryer body.
Using equation 1.1, it is possible to set a relation between the particle and droplet

$$d_{p,*} = \sqrt[3]{\frac{C_f}{\rho_p}} d_{D,*} \tag{3.39}$$

Where '$*$' could be any quantile. Assuming that the particle is completely dried after the droplet to particle transformation at the critical concentration, together with the mass conservation of the solid loading

$$\rho_p = \frac{m_{solid}}{V_{final}} = \frac{C_f \frac{\pi d_{initial}^3}{6}}{\frac{\pi d_{final}^3}{6}} = \frac{C_f d_{initial}^3}{d_{final}^3} \tag{3.40}$$

Inserting into 3.39 and simplifying leads to

$$d_{p,50} = \frac{d_{final}}{d_{initial}} d_{D,*}. \tag{3.41}$$

As $d_{initial} = d_{D,*}$, it is just to simulate the drying of the droplet with size $d_{D,*}$ to obtain the $d_{p,*}$. Another way to calculate $d_{p,*}$ from the results of the CDF calculations was be to perform sieve analysis calculation, find the index for which the cumulative volume fraction of the final particles > fraction for specific quantile. Then use the index value found in a linear interpolation to find the approximate $d_{p,*}$ value.

3.5.2 Specific surface area

Another measurement varaible suitable to use for parameter estimation is the specific surface area (SSA), which is the sum of all particle areas to their total weight in (m^2/g). It is possible to obtain an approximative value of the SSA assuming the final particle morphology stays spherical after the shell formation. This mean that any morphological evolution mechanisms such as buckling, inflation or shriveling are assumed to not influence real SSA. Since the hygroscopic nature of the material used in the experiments was low and the final product porous it enabled the assumption of full solvent evaporation to occur in the subsequent drying time left in the vessel. Then as motivated before the final particle mass of each particle would just become their initial solid loading.

$$SSA = \frac{\Sigma_i^n \theta_i A_i}{\Sigma_i^n \theta_i m_{particle,i}} = \frac{\Sigma_i^n \theta_i \pi d_i^2}{\Sigma_i^n \theta_i \frac{\pi}{6} \rho d_i^3} = \frac{\Sigma_i^n \theta_i d_i^2}{\Sigma_i^n \theta_i \frac{\rho d_i^3}{6}} \tag{3.42}$$

3.6 Numerical method

The model was evaluated in terms of time step, spatial discretization, numerical boundaries such as different droplet sizes and against an in-house model. Simulations

were performed on a tabletop computer, AMD Ryzen 5 PRO 5650U with Radeon Graphics.

3.6.1 Integration stepsize

Integration step size influence accuracy and efficiency to obtain numerical results. A lower integration step will increase the resolution of the solution, however will take more effort and computational time. In order to study the effect of the integration step size on the simulation results, a convergence study was conducted for pure solvent droplet diameter. The simulation results with different step sizes were later compared to an in-house model. The step size is not fixed, but set conditionally to be equal or below the 'maximum integration step' within the 'solutionparameter' of the differential algebraic solver for the process simulation in gPROMS. The time-step is adapted using the criterion

$$\epsilon_i < a + r|x_i| \tag{3.43}$$

Where ϵ_i is solver estimation of the local truncation error for the differential variable x_i, a is the absolute- and r is relative error tolerance (both set to 1E-5).

3.6.2 Simulation procedure

To comply with physical constraints the droplet/particle solvent leftover mass was checked at each iteration for conservation of mass according to

$$m_{solvent}(t) = m_{solvent,initial} - \int_0^t \dot{m}_{evap}\ \mathrm{dt} \tag{3.44}$$

as

$$m(t) > 0\ ,\ \forall t \geq 0. \tag{3.45}$$

The end condition in gPROMS was formulated simply in the process 'SCHEDULE', which was to continue the simulation for an arbitrary set time or stop when the condition

$$m(t) < 0 \tag{3.46}$$

was met. When introducing solid loading into the droplet this stop condition is not necessary as the solid material reaches a critical concentration and the drying stops, i.e. the solvent leftover mass would not become negative.

Figure 3.8 shows the droplet diameter trajectories for a simulation of a pure solvent water droplet with initial diameter 52 μm and 20°C T_{feed} and T_{gas}, with different maximum integration steps.

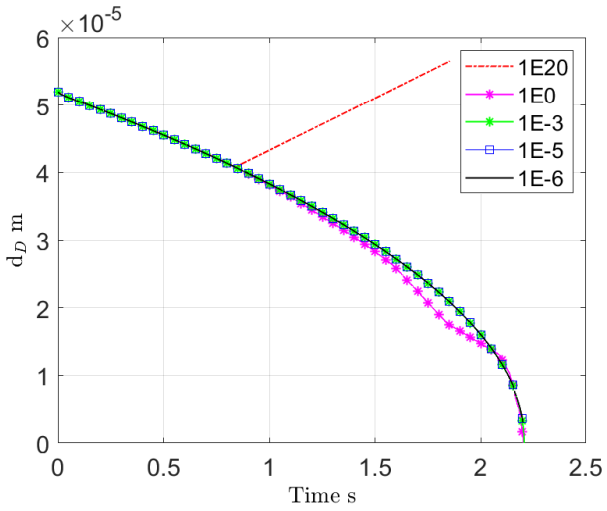

Figure 3.8: Droplet diameter predictions with different maximum integration steps

From figure 3.8, it is clear that the solution trajectory obtained with the maximum integration step up till 1E+20 and 1E0 deviates from the other chosen steps. Also the diameter results plotted here for max integration steps 1E-5 and 1E-6 do not go to zero, as the simulation stops abruptly when the droplet mass approaches values of 1E-17 and switches to 0.
The model performance was also evaluated against another model available in-house. Comparison on the diameter predictions were made using the error of the squared diameter, calculated in percentage as

$$\text{Error d}^2\ \% = 100 \cdot \frac{d_m^2 - d_{ih}^2}{d_{ih}^2} \tag{3.47}$$

Where the subscript, 'ih' is for the in-house model and 'm' is the built model.

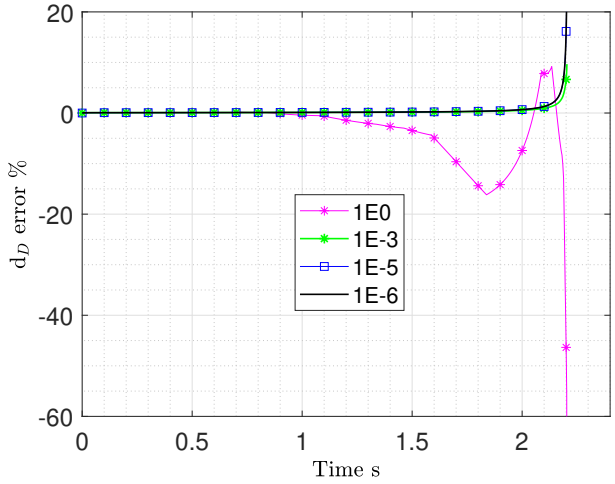

Figure 3.9: In house model comparison of droplet diameter predictions with different maximum integration steps

Both models make similar predictions of the diameter change, but close to the complete droplet evaporation the difference becomes asymptotic. Also nearing this limit gPROMS can not continue simulation due to the leftover solvent mass roundoff numerical error triggering the stop condition.

The combined results from figure 3.8 and 3.9 show that the range from maximum time step 1E-3 and lower is possible. Choosing the maximum integration step 1E-5, the simulations reach their stop condition when solvent droplet leftover mass is 0.0014 % of the initial droplet mass. The droplet diameter is 2.977E-6 m at time 2.2035 seconds, which is 5.7 % of the initial diameter. Figure 3.10a shows the droplet diameter prediction for maximum integration step 1E-5.

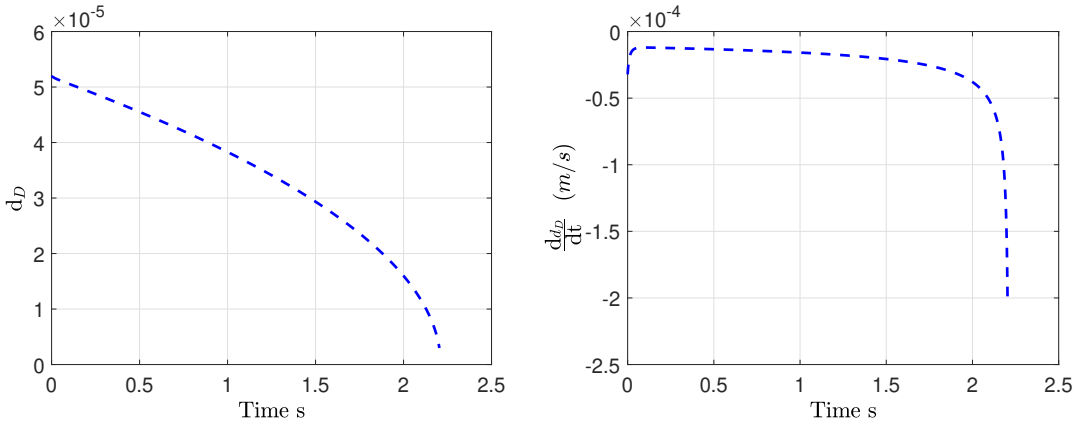

(a) Droplet diameter prediction **(b)** Rate of change droplet diameter

Figure 3.10: Prediction of droplet diameter and rate of change with maximum integration step 1E-5

In figure 3.10b it can be seen that the diameter changes rapidly in the beginning of drying and then moves to a slower changing rate. In the end of drying the droplet change becomes asymptotic as the equations no longer can describe the physical phenomena correctly.

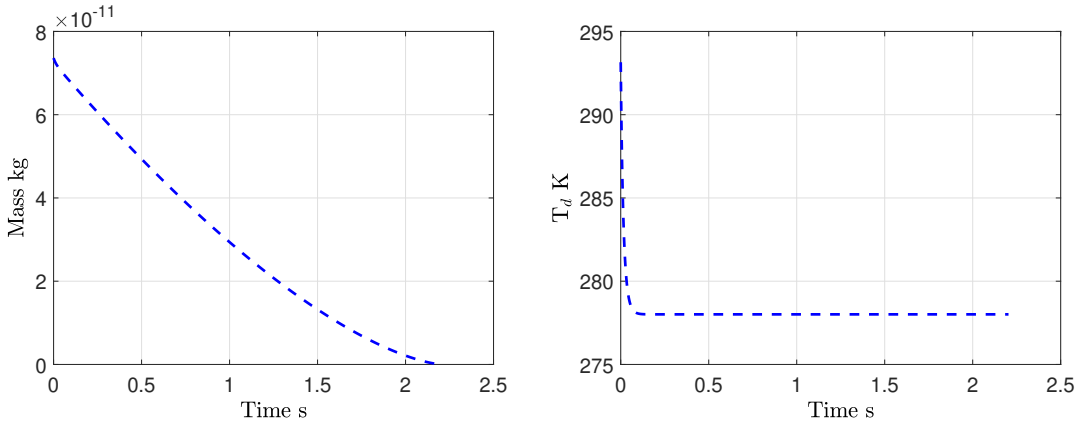

(a) Mass evolution **(b)** Temperature evolution

Figure 3.11: Evolution of mass and temperature of droplet with maximum integration step size 1E-5

Figure 3.11a and 3.11b show the mass and temperature evolution respectively for maximum integration step 1E-5. In figure 3.11b the temperature decreases towards T_{wb} of the drying system.
A comparison between the simulation trajectory of the droplet temperature was also made for the maximum integration step 1E-5 versus the in-house model, using the error calculated as

$$\text{Error } T_d \ \% = 100 \cdot \frac{T_{d,m} - T_{d,ih}}{T_{d,ih}} \tag{3.48}$$

.

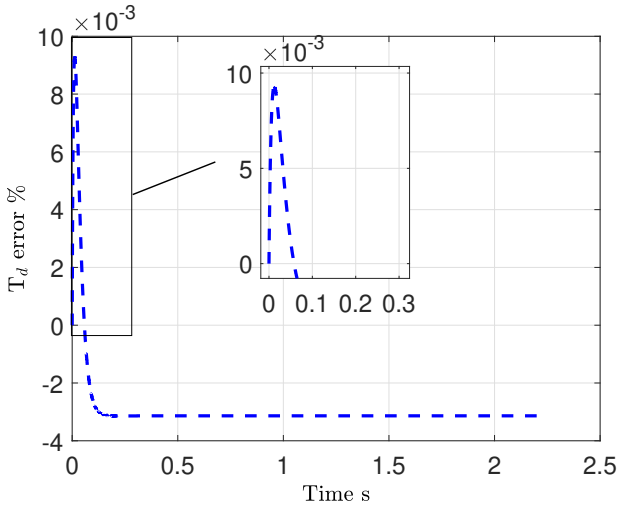

Figure 3.12: Model error temperature

From figure 3.12 it is seen that in comparison to the in-house model the model underestimates the heat loss of the droplet, and then switches to overestimate the loss. However, the absolute difference between both models is always below 0.01%.

3.6.3 Numerical integration

Simulating even finer sized droplets became a serious challenge for gPROMS. In SI units the numbers concerning the droplet physical attributes became extremely small oftentimes below 1E-14. This made numerical handling especially the numerical integration difficult with the integration stepsize sometimes being too small, ending simulations. So, in order to run with this setup, the reportinginterval had too be ever smaller leading to simulations taking much longer time. Therefore, in order to make numerical handling easier for gPROMS the equations used in the model implementation were nondimensionalized. The final non-dimensionalized equations implemented in the model are found in the appendix A.6.

3.6.4 Spatial discretization and numerical scheme

To solve the internal diffusion of solutes described by the second order partial differential equation numerically, the spatial domain of the particle must be discretized with a suitable numerical scheme. As the problem is solely dependent on diffusion and is without convective flow the second order centered finite difference method is used.

$$\frac{dC}{dz}(z_k) \approx \frac{C_{k+1} - C_{k-1}}{2h} + O(h^2)$$

The spatial domain was firstly described using an uniform grid (10, 100, 1000 points evenly spaced) along the radial axis to determine eventual strong gradients and to evaluate the speed of solution. Solving the governing equations at a denser grid will increase the resolution, but will also make the simulation slower.
Simulations at this stage were only performed seperately for excipients A and B. Excluding the solutes, the simulation process conditions are stated in table 3.3.

Table 3.3: Process conditions for the simulation

$d_{D,initial}$ (μm)	T_{feed} (°C)	T_{amb} (°C)	Y (kg_w/kg_{N_2})
52	20	20	0

The initial solvent droplet mass was 7.36E-11 kg. The stop criteria for the simulations was the critical concentration of either components. From the difference in spatial resolution between the simulations the stop conditions were met at different times. A grid refinement study was conducted to measure solution quality with increasing grid refinement.

Table 3.4: Simulation with uniform grid with excipient A (initial loading ■ mg/ml), SI based model

Grid points	$t_{simulation}$ (s)	CPU (s)	$t_{C_{crit}}$ (s)	diameter (μm)
10	33.4	32.0	1.65771	25.8815
100	77.7	76.2	1.65976	25.8333
1000	1110.0	1101.8	1.65977	25.8331

Nondimensionalized model results

Table 3.5: Simulation with uniform grid with excipient A (initial loading ■ mg/ml), Nondimensionalized model

Grid points	$t_{simulation}$ (s)	CPU (s)	$t_{C_{crit}}$ (s)	diameter (μm)
10	1.4	0.3	1.65890	25.8815
100	1.1	0.9	1.66095	25.8334
1000	10.0	9.8	1.66096	25.8332
10000	85.9	85.7	1.66096	25.8332

Comparing the simulation results of the SI and nondimensionalized models, it is clear that the speed of simulation is greatly impacted. Also to compare the in-house model, the exact same simulation for excipient A loading took $t_{simulation} = 25.6383$ s and reaching the critical concentration $t_{c_{crit}} = 1.6821$ s The simulation results for excipient B with both the SI and nondimensionalized model can be found in A.6.

Using the grid convergence index (GCI) for uniform grids developed by Roache [53], tells how far the numerical solution is from the asymptotic numerical value in percent. GCI for the fine grid is defined as

$$GCI_{fine} = \frac{F_a|\epsilon|}{r^p - 1} \tag{3.49}$$

Where F_a is the factor of safety, which for comparison of three different grids is 1.25.

$$\epsilon = \left| \frac{f_1 - f_2}{f_1} \right| \tag{3.50}$$

The simulation value f is obtained for the corresponding grid, where subindex 1 is the densest and 3 is the coarsest. Here, r is the grid refinement ratio, in this case constant 10 as the grid points increase tenfold each refinement.

The order of convergence p,

$$p = \frac{ln(|\frac{f_3 - f_2}{f_2 - f_1}|)}{ln(r)} \tag{3.51}$$

Evaluating GCI with the corresponding values from table 3.5, GCI =6.95E-8, which shows that the difference between the medium and finest mesh is minuscule and that they are both close to the asymptotic value [53–55].

Simulation results of the droplet loaded with ■ mg/ml excipient A in a uniform 1000 point grid are used to visualize the evolution in radial distribution of concentration and the surface concentration, see figures 3.13 and 3.14.

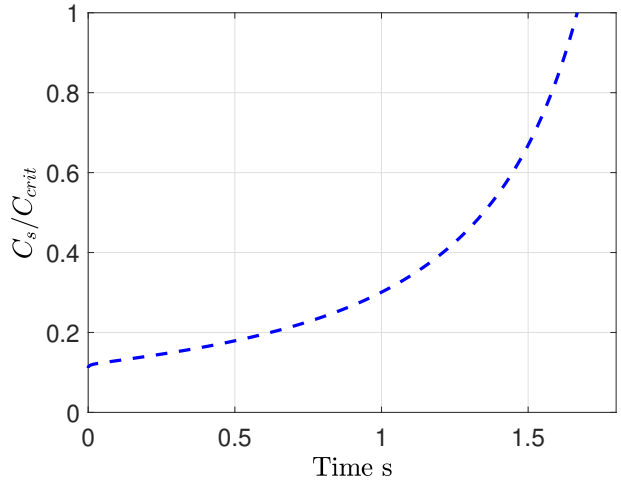

Figure 3.13: Time evolution of excipient A surface concentration normalized with critical concentration

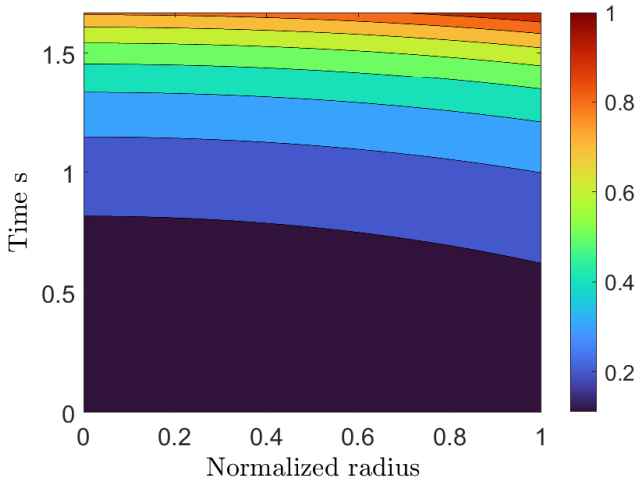

Figure 3.14: Contourplot of excipient A concentration normalized with critical concentration, radial distribution with time

To conclude, analysis of results from figure 3.14 the uniform grid makes clear that the steepest concentration gradients are at the surface, r=1. Adjusting the grid points via a exponential transform leads to non-uniformely spaced grid points being concentrated towards the particle/droplet edge.

$$\hat{z} = \frac{e^{az} - 1}{e^{a-1}} \tag{3.52}$$

Where $\hat{z}$ is the new position of the grid point, and z is the old grid uniform grid point position. The exponential transform coefficient a and the number of grid points were also evaluated, see tables A.3 and A.4. Shifting to a non-uniform mesh leads to higher resolution on the edge with fewer grid points than a refined uniform mesh. Also considering, from a theoretical viewpoint that the shell is always initiated at

the surface, the spatial focus should be towards the edge. What is occurring within the droplet is of 'less' importance. Henceforth the non-uniform grid with 100 points and a=4 was chosen for simulations, with maximum integration stepsize set the default interval 1E20 to 1E-20.

3.7 Parameter Estimation

Non-dimenzionalizing the model lead to fast and robust simulations of the droplet drying. This enabled parameter estimation simulations to be performed for the critical parameters that could affect shell formation. gPROMS model validation tool was used to fit equation parameters to data.

3.7.1 Estimation of heat loss

The heat transfer coefficients of both the pipe and dryer body are parameter estimated to match the real exhaust temperature of the system from experiments using gPROMS model validation. gPROMS employs the use of the maximum likelihood method, which simultaneously estimate parameters within the model and the variance model describing accuracy of measurements. In this setting constant variance is applied assuming the accuracy of the equipment measurement of temperature to be within ± 1K.
The data which the model validation uses are the performed experiments from different spray dryer settings. Inlet conditions for the dryer ($T_{in,dg}$, $T_{in,ag}$, $T_{in,feed}$, $\dot{m}_{dg}$, $\dot{m}_{ag}$, $\dot{m}_{feed}$) and the ambient condition (T_{amb}) provide time-invariant control variables, as they are not changed during the experiment. Whereas the measured data is the outlet temperature $T_{gas,out}$, and the heat transfer coefficients parameters to be estimated are set with initial guess values. MLE finds the most likely pair of heat transfer coefficients from the equations which give the real $T_{gas,out}$.
To handle more general cases of drying such as moist drying- or atomizer gas at the inlet the equation for drying without solids 3.37 is slightly refined as A.19. For the case with solids the entire equation A.19 describing drying is rewritten in terms of free solid moisture content X in equation A.20. Where X is assumed to be in equilibrium with the gas moisture, sorption equilibrium isotherm.
Experimental data of moisture content of wet basis (kg wet / kg total),

$$x = \frac{m_{wet}}{m_{dry} + m_{wet}} \tag{3.53}$$

corresponding to relative humidity was available. To be used in equation A.20 the moisture content of wet basis x was translated to moisture content on dry basis X using

$$X = \frac{x}{1 - x} = \frac{\text{kg wet}}{\text{kg dry}} \tag{3.54}$$

The moisture in the solids are assumed to be in equilibrium with the gas moisture. Using supplied results of moisture sorption isotherms, the moisture content on dry basis was linearly fitted against the relative humidity values using matlab curve fitter tool, see appendix A.2.1.

The relative humidity, equation 1.7, that was used in A.2.1 was supposed to be calculated with the partial solvent vapor pressure 1.8 and P_{sat} from an Antoine equation. However, the parameter estimation failed when using solid content based equations with the Antoine equation describing the saturation pressure, even though the original problem was well posed, gPROMS was unable to perform initialization calculations.Instead of describing the saturation pressure with an Antoine expression, the saturation pressure was fitted with a polynomial expression of temperature with matlab curve fitter, see A.2.2 The respective values of P_{sat} and T were taken from an engineering table [56] for air.

3.7.2 Estimation of critical concentration

The formulations within the experiments included API, buffer and excipients A, B and C. Also, the API and buffer used in the system respective critical concentration and diffusion (molecular radius) were unknown. Leading to a problem where one had to simultaneously perform parameter estimation for C_{crit} and diffusion, generating a system which probably would be too highly correlated. For this reason, a stepwise approach was used to deal with uncertainty associated with interactions between the components. Within the scope of the thesis, the main interest was put on seperately estimating diffusion and critical concentration of excipient A. The reason for this choice is that excipient A is known from literature to be one of the primary shell formers in a formulation, or atleast highly impacting the shell formation, as it is a surface active compound.
The parameter estimations of excipient A diffusion and critical concentration were firstly performed in a generic format, where each of the components surface concentration could influence the droplet to particle transition. In the respective case the literature values of C_{crit} and the Stokes-Einstein diffusion was used. (Components without a description of C_{crit} and/or diffusion were assigned an arbitrary value of 1000 mg/ml and the same molecular radius as excipient A). The diffusion was parameter estimated as a multiplicatory factor, $D_{constant,i}$ as,

$$D_{\text{component,i}} = D_{\text{constant,i}} \cdot \frac{k_B T}{6\pi\mu_w R_A}. \tag{3.55}$$

However, this method risks inconsistency, as some component other than excipient A potentially could reach the C_{crit} faster when the corresponding value of excipient A was evaluated at higher ranges. In order to resolve this, but still in the general format, a double safety margin (DS) was used which meant that the other components diffusion constants were taken as $D_{constant} = 1000$. Also, the other components respective critical concentrations were all increased to 1E6 mg/ml.
Considering the diffusion, the larger it would be, the faster the solutes would travel into the core of the droplet during drying. Furthermore, heightening the critical concentrations of the components make their respective crust formations less likely to occur. Atleast, this should be the case when choosing the parameter estimation of $C_{crit,A}$ to live in a reasonable domain close to the known literature value. Tables 3.6 and 3.7 show the model validation setup with double safety margin for the diffusion coefficient and the critical concentration respectively. The model validation is

done separately with each parameter. Observe that the parameter to be estimated '$D_{constant}$' is each respective components multiplicatory factor, not the diffusion coefficient. The diffusion coefficient is evaluated with equation 3.55. $D_{constant}$ is unitless, C_{crit} has units kg/m^3.

Table 3.6: Model validation setup for excipient A diffusion coefficient, with double safety margin

Parameter to be estimated	Initial guess	Fixed?	Lower bound	Upper bound
$D_{constant,API}$	1E3	✓	-	-
$D_{constant,Buffer}$	1E3	✓	-	-
$D_{constant,A}$	1E3		1E-3	1E3
$D_{constant,B}$	1E3	✓	-	-
$D_{constant,C}$	1E3	✓	-	-
$C_{crit,API}$	1E6	✓	-	-
$C_{crit,Buffer}$	1E6	✓	-	-
$C_{crit,A}$	18	✓	-	-
$C_{crit,B}$	1E6	✓	-	-
$C_{crit,C}$	1E6	✓	-	-

Table 3.7: Model validation setup for excipient A critical concentration, with double safety margin

Parameter to be estimated	Initial guess	Fixed?	Lower bound	Upper bound
$D_{constant,API}$	1E3	✓	-	-
$D_{constant,Buffer}$	1E3	✓	-	-
$D_{constant,A}$	1	✓	-	-
$D_{constant,B}$	1E3	✓	-	-
$D_{constant,C}$	1E3	✓	-	-
$C_{crit,API}$	1E6	✓	-	-
$C_{crit,Buffer}$	1E6	✓	-	-
$C_{crit,A}$	18		15	1E2
$C_{crit,C}$	1E6	✓	-	-
$C_{crit,B}$	1E6	✓	-	-

One caveat of the parameter estimation is that it uses the experimental data of the SSA at a specific set time for total simulation time and evaluation. Therefore in order to fully control the precision of the parameter estimation, the measurement time must be accurate to allow for the entire system to dry. However, it was not found possible to use a generic way, such as a break-condition when the internal process simulation has finished for the time of evaluation. Also, setting the time based upon some earlier simulation results would not work either, as the parameter estimation variables change the dynamics of the system. Therefore drying of the largest droplets might not have proceeded 100%, as the time listed in the experiments could be lower. However, with a sufficiently large arbitrary time taken this should

not have that large of an impact when calculating the SSA, as the largest droplets have a lower area to volume ratio than smaller droplets. The influence of the SSA is mainly from the small particles. Also, from the particle size distribution there are fewer droplets of the large droplet size in comparison to the small droplet sizes.

4

Results

4.1 Validation of drying model

The model's performance is assessed with the experimental data of water droplet drying produced by [41], see figure 4.1. The model initial conditions are set to those of the experiment, initial droplet size is 52 μm, inlet temperature of water is 20°C, drying gas temperature either 8 or 20°C, the drying gas absolute humidity is assumed to be zero as the amount of gasflow is significantly higher. The drying gas used in the experiments was air, but in the model the drying gas is simulated as pure nitrogen with corresponding transport coefficients for a water-nitrogen system.

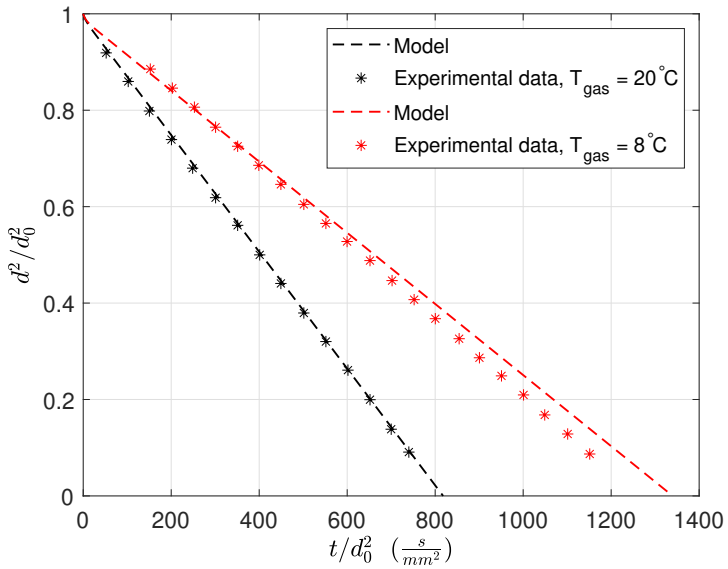

Figure 4.1: Model results against experimental data from [41]

From figure 4.1 it can be seen that the model follows the experimental results for the T_{gas} = 20°C case quite well. For the other case, the model deviates from the experimental values. This is probably due to a combination of assumptions made formulating the model (e.g. quasi-steady state derived heat balance) and material properties. Also, the wet bulb temperature T_{wb} reached in this case was 271.6 K, changing the dynamics of the droplet drying system from two phase to three phase. Nevertheless it can be concluded that the model is implemented appropriately and show predictability with experimental results.

4.2 Heat loss in spray dryers

Parameter estimation of convective heat losses of the MS35 dryer were performed on experimental data of spray drying cases run in complete dry state without droplets being dried (just atomizer and drying gas flow) and for wet condition with both atomizer and drying gas with liquid solvent feed without dissolved solids. Figure 4.2a show the parity plot of the parameter estimation, whilst fig 4.2b show the external validation using equation A.19.

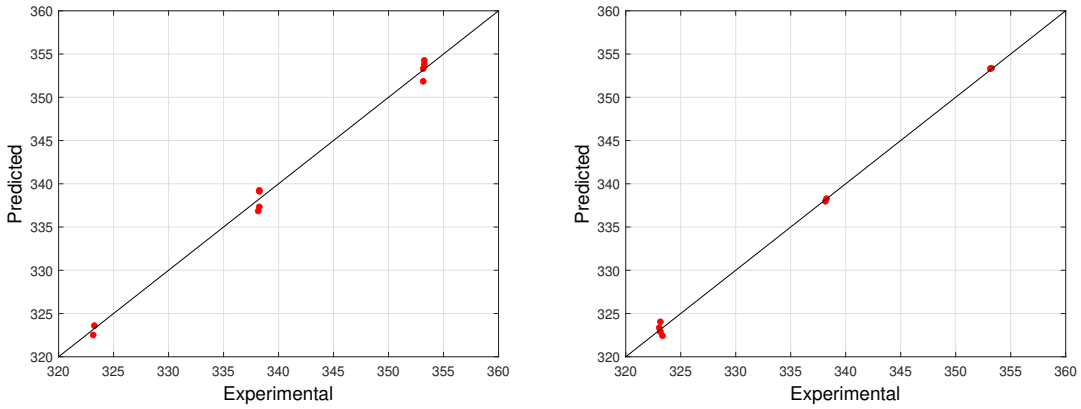

(a) Parameter estimation **(b)** External validation

Figure 4.2: Heat loss model validation results for MS35 spray dryer without solid loading, represented as temperature parity plots

The parity plot in figures 4.2a and 4.2b comparing the results from the parameter estimation of the heat loss coefficients to the real experimental results shows that the prediction is valid, as the data produced by the model falls on the diagonal reference. From the parameter estimation of without solids, the RMSE $\approx$ 0.886. Which gives that 95 % observed temperature outlet values are within the range 1.77 K of the predicted values. Performing parameter estimation using MS35 experiments without solid loading showed consistent results using both equations A.19 and A.20. The values of h_{pipe} and h_{body} attained is shown in table 4.1, with a caveat that the t-value for h_{pipe} 1.61 is below its 95 % reference value 1.75.

Table 4.1: Heat loss constants without solids

Dryer	h_{pipe} (W/K)	h_{body} (W/K)	RMSE
MS35	0.96	3.90	0.73

Using the heat loss constant from the parameter estimation the temperature predictions are calculated for each dryer setup. The temperature prediction is shown as Residual = Predicted - Experimental, see figure 4.3.

Figure 4.3: Exhaust temperature prediction in terms of residuals for MS35 dryer without solid loading

However, the heat loss constants derived from parameter estimation without solid could not be used to describe the heat loss constants for the solid loading case, as seen from the external validation in figure 4.4. For this case, the calculated RMSE was 6.40.

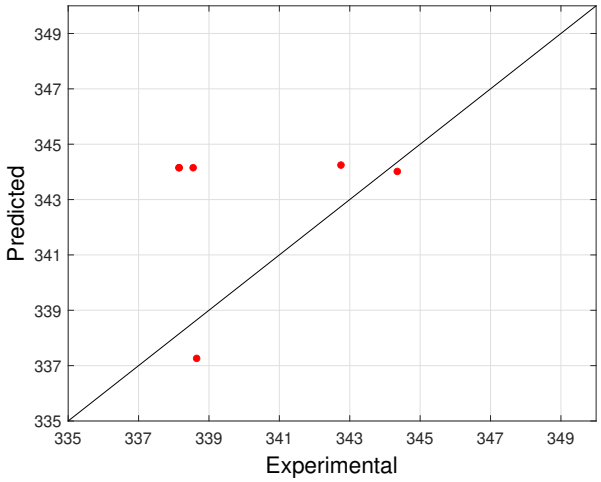

Figure 4.4: External validation for MS35 spray dryer (solid loading) in terms of temperature parity plot to evaluate if the heat loss constant derived without solid loading is good predictor also for solid loading case

Parameter estimation of heat loss coefficients for experiments run with solid content using both the simple and more sophisticated equations A.19 and A.20 gave consistent results. AZ and Buchi are assumed to not have any pipe loss, therefore $h_{pipe} = 0$ in table 4.2.

Table 4.2: Heat loss constants with solid loading

Dryer	h_{pipe} (W/K)	h_{body} (W/K)	RMSE
AZ	0	1.90	1.64
Buchi	0	5.6	0.74
MS35	0	6.05	5.84

gPROMS excluded the analysis of h_{pipe} for MS35, therefore it is set as 0. The results from table 4.2 show that the parameter estimation of heat loss constants to fit the exhaust temperature is quite poor for MS35 in the case with solid loading, as the RMSE value is high making the approximate 95 % prediction interval ±11.7 K. The parameter estimation and exhaust temperature predictions for AZ, Buchi and MS35 spray dryer with solid loading can be seen in figures 4.5, 4.6 and 4.7 respectively.

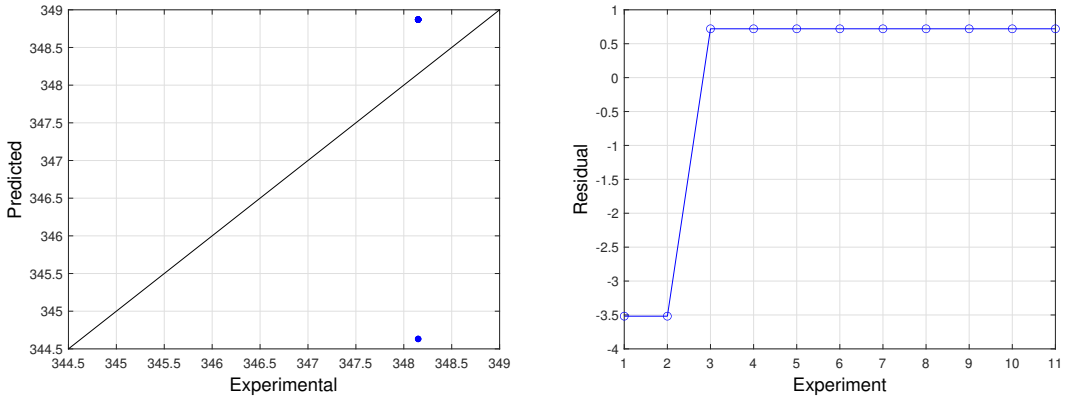

(a) Parameter estimation, temperature parity plot

(b) Exhaust temperature prediction in terms of residuals

Figure 4.5: Heat loss model validation for AZ spray dryer with solid loading

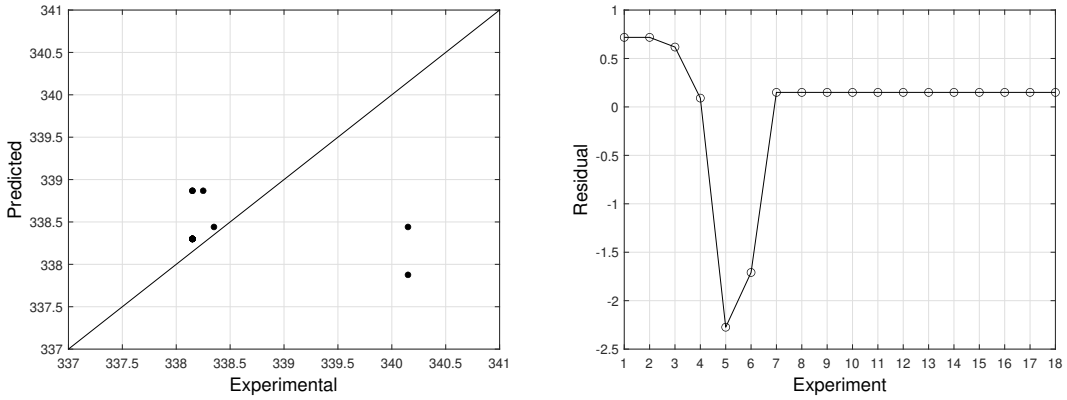

(a) Parameter estimation, temperature parity plot

(b) Exhaust temperature prediction in terms of residuals

Figure 4.6: Heat loss model validation for Buchi spray dryer with solid loading

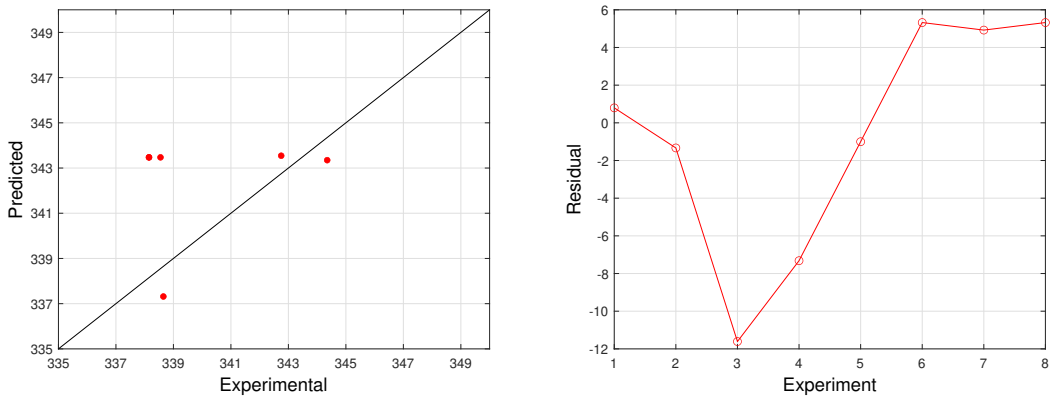

(a) Parameter estimation, temperature parity plot

(b) Exhaust temperature prediction in terms of residuals

Figure 4.7: Heat loss model validation for MS35 spray dryer with solid loading

4.3 Influence of diffusion coefficient calculation on shell formation

To observe the influence of the diffusion description of excipient B has on the surface concentration trajectory, a simulation of the constant diffusion coefficient found in literature and another with the Stokes-Einstein equation were compared. Simulation of 52 μm droplet, with 20°C T_{feed} and T_{gas}.

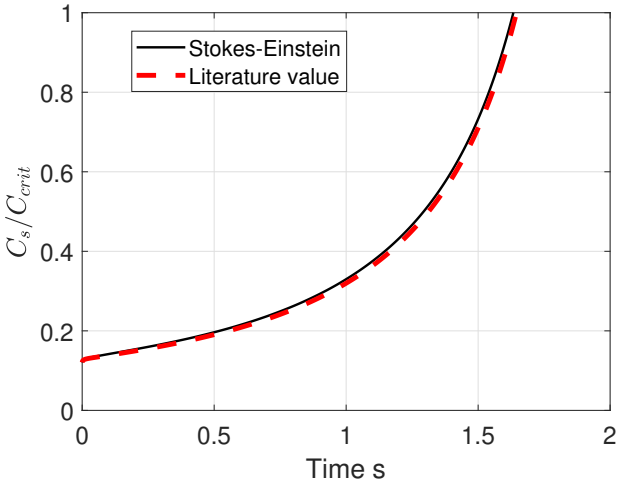

Figure 4.8: Normalized surface concentration of excipient B, diffusion described with Stokes-Einstein equation and constant value from literature

From figure 4.8 it can be seen that the solution trajectory of the surface concentration with the two diffusion descriptions are close. The average value of diffusion taken from the Stokes-Einstein equation at the constant drying rate at $T_{w,bulb}$ of the droplet $D_{excipient,B}$ was close to the literature value.

The sensitivity analysis was also performed for excipient Aon an entire system of droplets drying within a chosen Buchi spray dryer experiment, which is more relevant both on a size and time scale for this spray drying application. Since no literature value for excipient A was available, the value for excipient B was used. Running the total system to complete drying with the literature value of diffusion contra the Stokes-Einstein gave a relative difference of 0.5% for the SSA (with Stokes-Einstien as reference).

The figure 4.9 show the normalized surface concentration evolution for some different initial droplet sizes with the two diffusion definitions. It can be observed from the figures that the definitions give no significant difference.

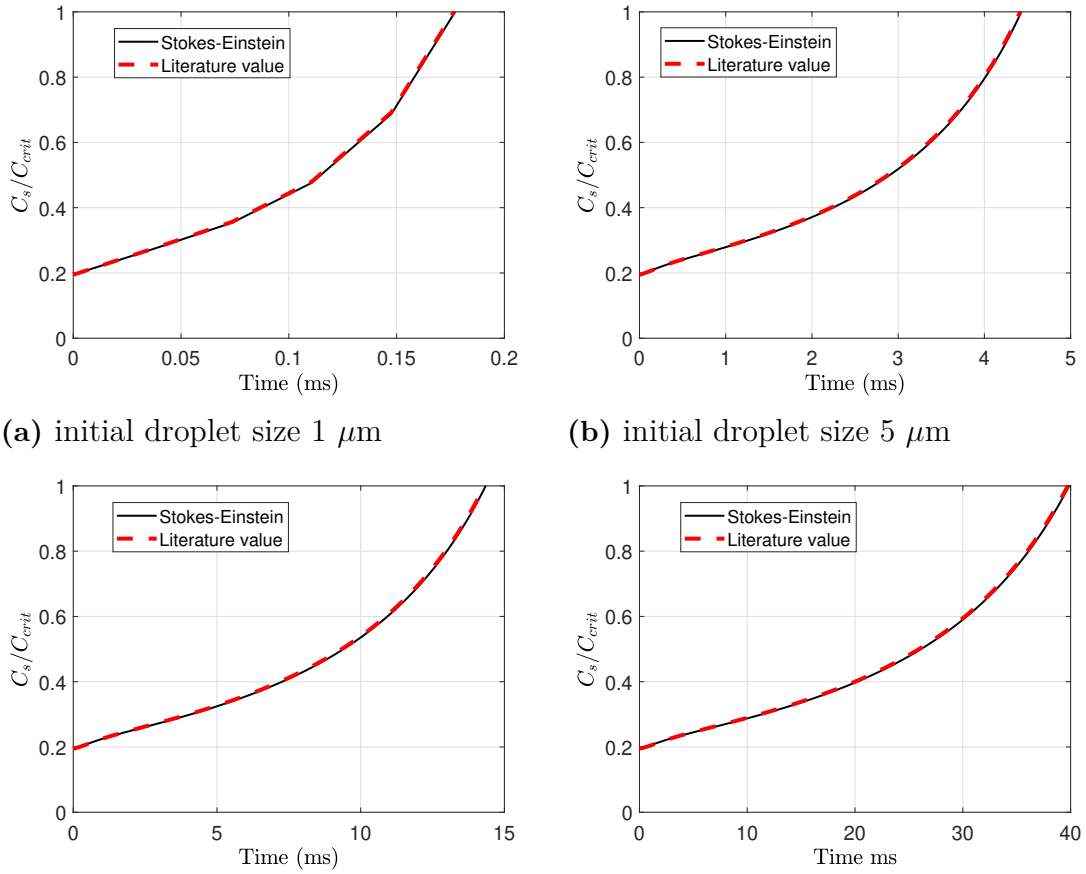

(a) initial droplet size 1 μm

(b) initial droplet size 5 μm

(c) initial droplet size 9 μm

(d) initial droplet size 15 μm

Figure 4.9: Normalized surface concentration of excipient A with different intial droplet sizes

The evolution of the diffusion coefficients for two different droplet sizes are shown in figure 4.10. From these figures it can be observed that the change in diffusivity occurs rapidly at the sensible heating towards $T_{wb} \approx 296$K, resulting in a diffusion coefficient $D_{excipient,A}$ rather close to the literature value. Thus, the diffusion coefficients from the two definitions do not show significant difference.

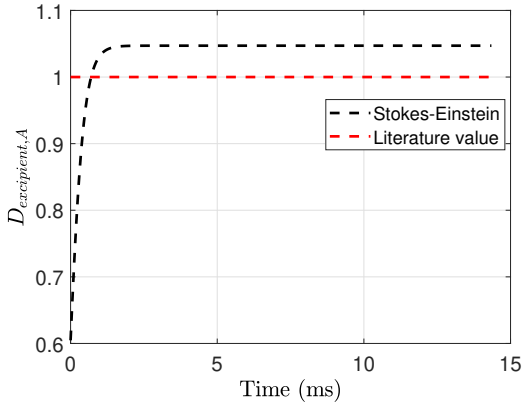

(a) initial droplet size 9 μm

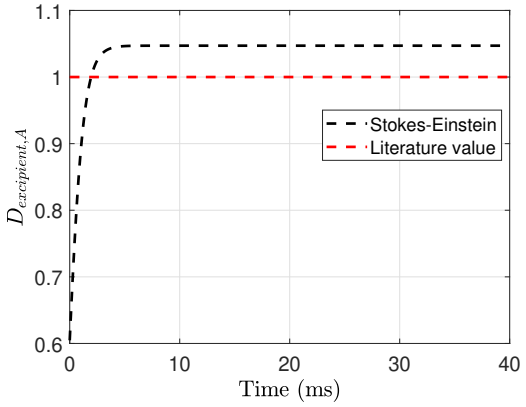

(b) initial droplet size 15 μm

Figure 4.10: Evolution of diffusion coefficient with different initial droplet sizes, both of the diffusion coefficients are normalized with the literature value

From the definition of the Stokes-Einstein diffusion, the diffusion follows the temperature trajectory strongly, via the pure solvent viscosity, see figure 4.11a and 4.11b.

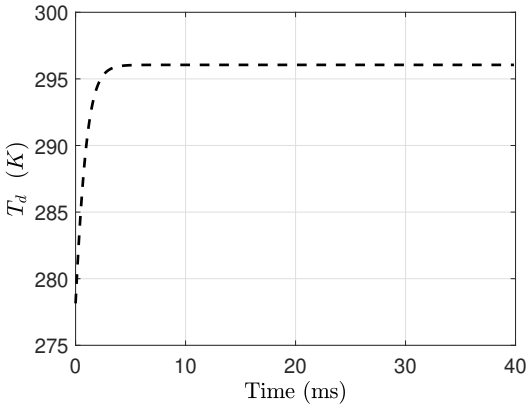

(a) temperature evolution

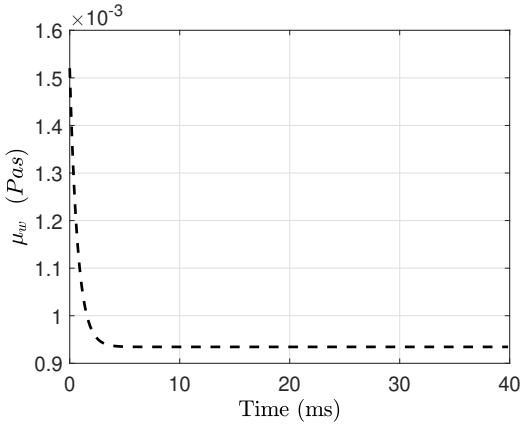

(b) viscosity evolution

Figure 4.11: Droplet temperature and viscosity evolution, initial droplet size 15 μm

4.4 Prediction particle size

To visualize the prediction of particle size, one experiment of each respective dryer was used. Internal diffusion was defined by Stokes-Einstein equation and critical concentrations by the literature values. Figures 4.12a, 4.13a and 4.14a below show the inlet PSD (the droplet size distribution calculated with the atomizer model) versus the final outlet PSD for the dried particles. Figures 4.12b, 4.13b and 4.14b show the corresponding volume fraction per particle size for the final dried particles. It is clear from the figures that the size distribution as well as the volume fraction is shifted to the smaller particle sizes by drying. Compare with the volume fraction per droplet size diameter in the Atomization model section, 3.3.1.

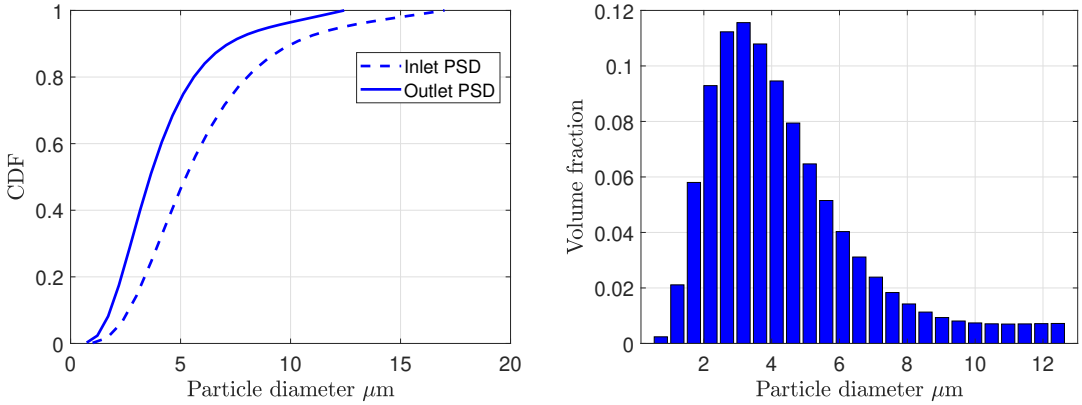

(a) Particle size distribution **(b)** Volume fraction per particle size

Figure 4.12: AZ dryer prediction of particle size

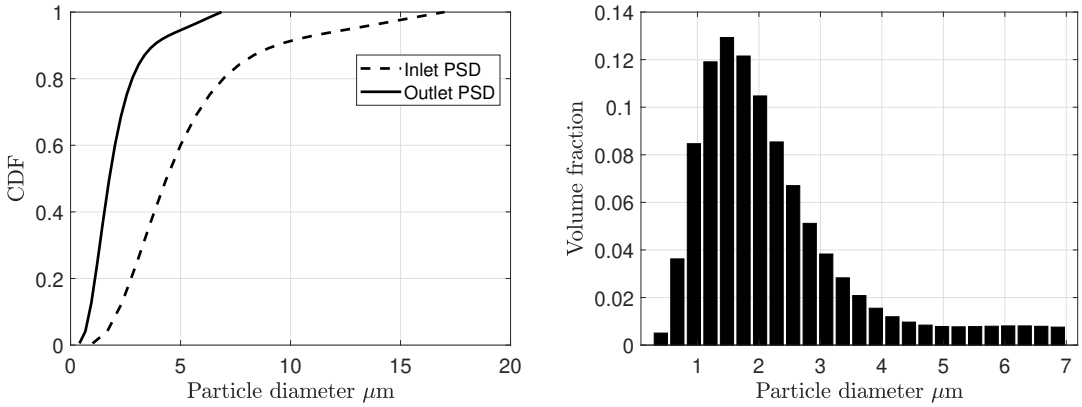

(a) Particle size distribution **(b)** Volume fraction per particle size

Figure 4.13: Buchi dryer prediction of particle size

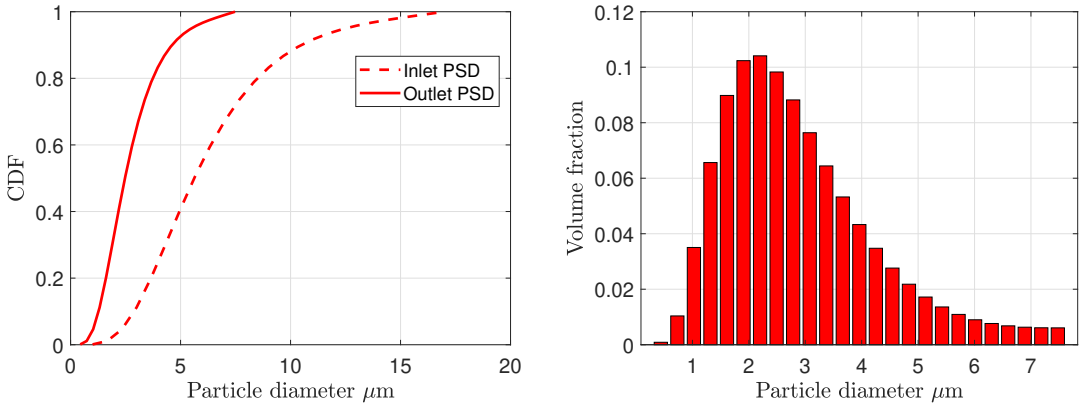

(a) Particle size distribution **(b)** Volume fraction per particle size

Figure 4.14: Buchi dryer prediction of particle size

4.5 Prediction of Specific surface area

To visualize the model performance in predicting the SSA value an external validation running all the experiments with their respective process conditions and feed formulations was performed. The model had the diffusion described by the Stokes-Einstein equation and critical concentration values found in literature. The results were mainly analyzed from the parity plot, residual and NRMSE calculations. The simulation results of the experiments run with the model is shown in the external validation parity plot in figure 4.15.

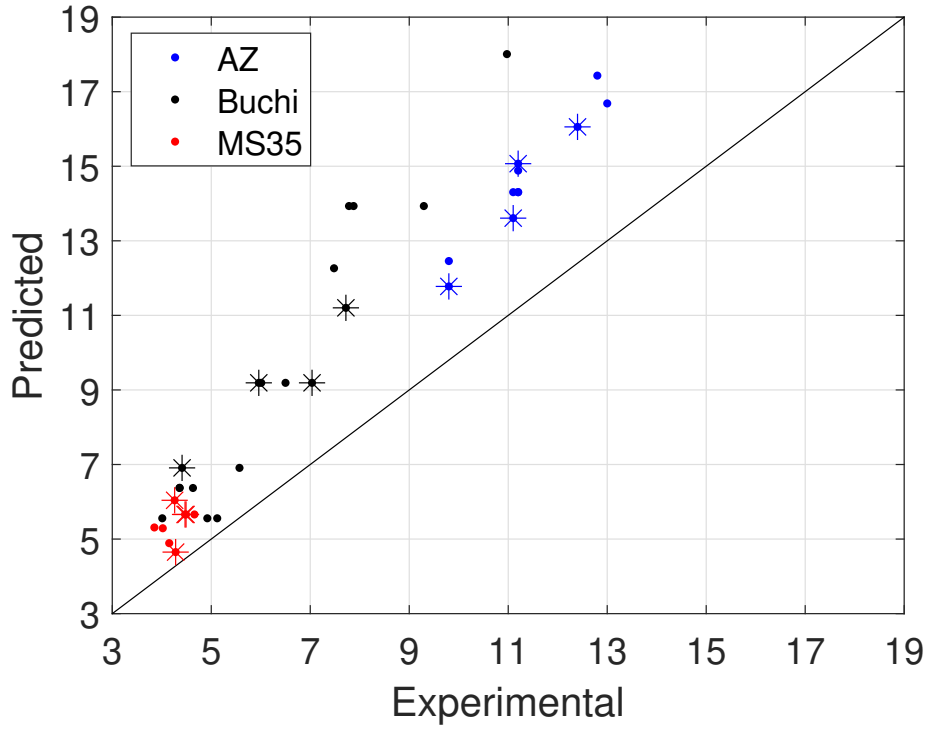

Figure 4.15: External validation of model performance in predicting the SSA

It can be seen that the model consistently overpredicts the SSA in comparison to the experimental results. In addition to these observations, it was confirmed with the separate simulations of the experiments that the primary shell former always was excipient A. In combination, these results suggest that parameter estimation of critical parameters eg. critical concentration (likely to be decisive for the onset of shell formation and in turn SSA) is possible.

The experiments used for the parameter estimation later for each dryer type is showed with an asterix, $*$. Figure 4.16a show the residual plot, where Residual = Experimental - Predicted. Figure 4.16b depicts the results from the NRMSE calculations visaulizing that the experiments done by MS35 is best described by the model.

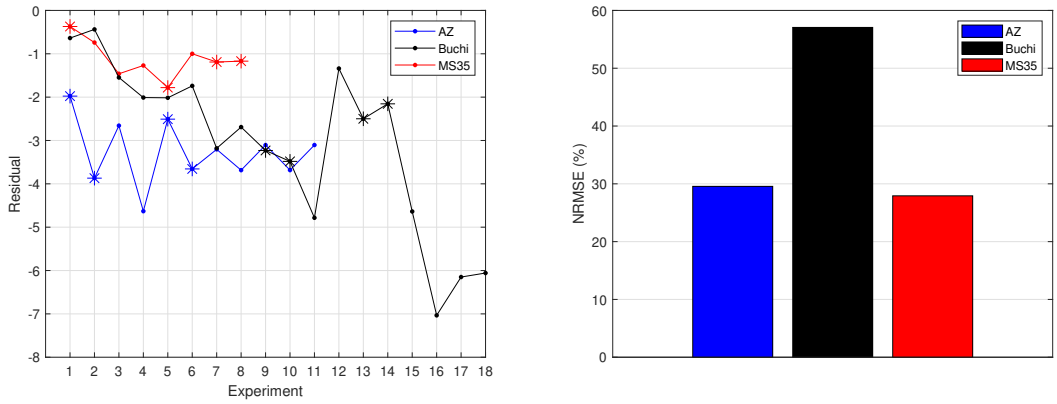

(a) Residual plot **(b)** NRMSE for dryers

Figure 4.16: Residual and NRMSE analysis from results of external validation

To use SSA as a measurement variable is advantageous because the particle size distribution is towards the smaller particle sizes, as seen from the particle size predictions in section 4.4. Also, it is reasonable to argue that geometrical attributes of small particles after shell formation are mildly affected by deformation or other morphological mechanisms. In addition, large particles are likely to have less effect on overall SSA. The reason against using specific sizes or size distribution quantiles, eg. d_{50} for measurement variables in model validation is the lack to accurately describing the geometrical particle evolution in simulations and possible error induced in experimental measurement analysis. The analysis of powder properties is oftentimes handled with image analysis and necessitates that the powder sample examined is representative for the whole batch size distribution. Also geometrical properties of particles which are not spherical are registered by orientation averaging. Other measurement techniques, eg. optical use equivalent diameters, where reference geometries need to have the same measurement properties of the particle evaluated to be accurate [1].
It should also be noted that parameter estimation with a theoretical model of the drying scenario risks overlooking other physical moisture transport mechanisms, as it is seldom that only one transport mechanism dominates the whole process. Adjusting transport phenomena coefficients such as diffusion may drive the theoretically defined model to approach experimental results, even though the model in reality isn't valid, good enough or the variable don't have any larger control of the system [57].

4.6 Predicting droplet to particle transition

Results from experimental data and literature suggest that SSA has potential of quantifying the onset of shell formation. Also, the assumptions that SSA is mildly affected after shell formation in the second drying stage are supported by earlier in-house results. These prove good agreement of predicted to experimentally measured SSA (by Brunauer–Emmett–Teller analysis (BET)) from similar spray drying systems. From the previous section, external validation results with the critical

concentration value of excipient A from literature gave consistent over-prediction of SSA. This motivates a search of an improved estimation of the critical concentration.

From the external validation of the unaltered model four experiments from each dryer setting (AZ, Buchi, MS35) were chosen for parameter estimation of diffusion and critical concentration of excipient A, see figures 4.15 and 4.16a.

As mentioned in the method section, it was found out that other components than excipient A potentially could influence the results of the parameter estimation. Therefore parameter estimation was run with two cases, the 'original' (where all components could infleunce) and with double safety (DS), (see method section). The parameter estimation of the diffusion constant for the two cases gave the same results, where gPROMS only performed two step evaluations. However, the resulting $D_{constant}$ had huge 95 % confidence interval and standard deviation, meaning that the accuracy of the estimation was poor, see table 4.3.

Table 4.3: Parameter estimation of the multiplicatory diffusion factor with the original and DS case

Case	Final value	95 % confidence interval	Standard deviation
Original	500	170753	77580
DS	500	171071	77725

See table 3.6 for the model validation setup with double safety margin.

For $C_{crit,A}$ the two setups consistently estimated final values, supported by the small difference in confidence interval and standard deviation in table 4.4. There was a small difference which is likely due to that some component other than excipient A influenced the outcome. From these results, its possible to estimate that $C_{crit,A} \approx 29 \pm 4$ mg/ml, see table 4.4. This value was used for further evaluation.

Table 4.4: $C_{crit,A}$ from parameter estimation

Case	Final value	95 % confidence interval	Standard deviation
Original	29.36	4.27	1.94
DS	29.26	4.22	1.92

Figure 4.17 shows the parity plot of SSA from parameter estimation of $C_{crit,A}$, using values from the DS case (see table 3.7).

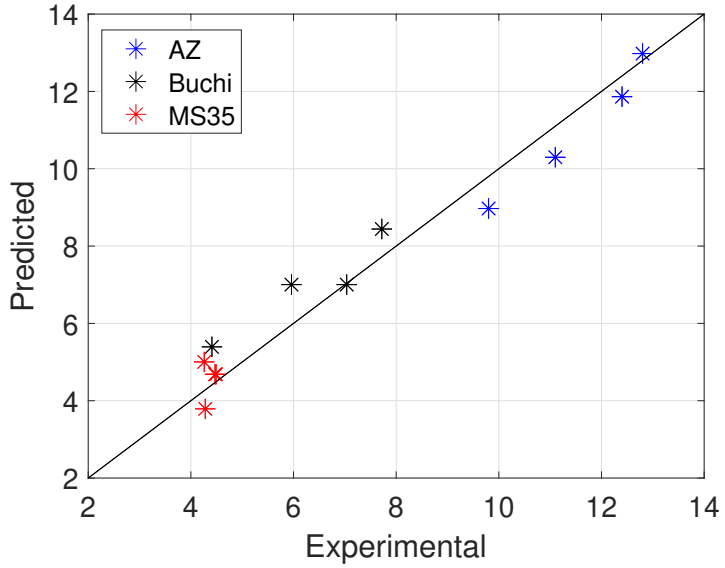

Figure 4.17: DS Parameter estimation of $C_{crit,A}$ for predicting the SSA

These results show that the parameter estimation of critical concentration using a small subset of spray drying experiments across spray dryer scales give good prediction of SSA. Figure 4.18 show the parity plot of SSA for external validation validation points, using values from the DS case.

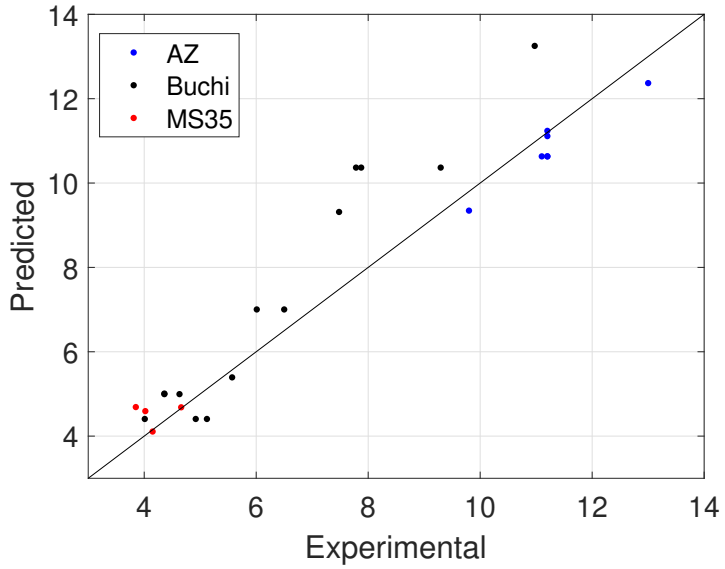

Figure 4.18: External validation to predict SSA with $C_{crit,A}$ from parameter estimation

The validation points also show good alignment of the predicted versus experimental data.
Figures 4.19a and 4.19b show the residual (measured-predicted) of the SSA and the NRMSE for each dryer type.

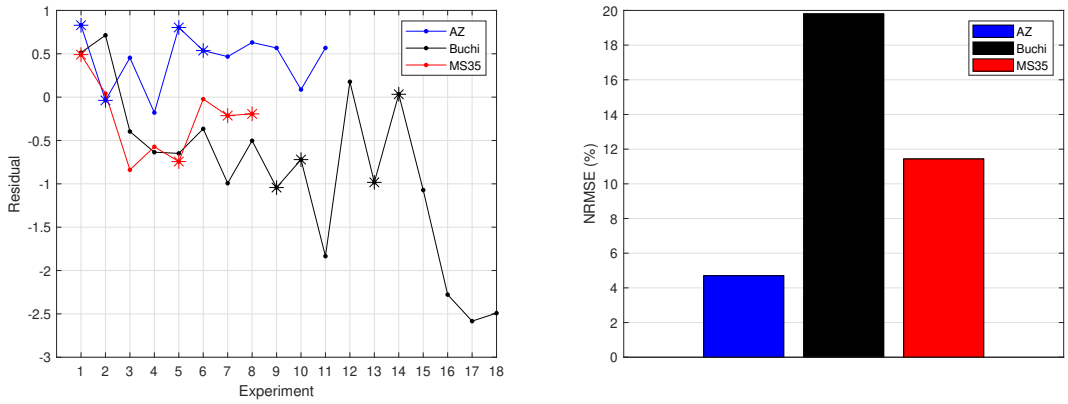

(a) Residual **(b)** NRMSE

Figure 4.19: Analysis of external validation results

The results show that the critical concentration derived from parameter estimation give best predictions for the AZ spray dryer. The residual for both AZ and MS35 are low, however this is not true for Buchi. As the RMSE is sensitive to outliers, the prediction accuracy for Buchi might be affected disproportionally from eventual outliers (experiment 16,17,18).

The results of the parameter estimation of the diffusion constant (DS case) in figure 4.20 indicate that the diffusion is not dominant in describing onset of shell formation.

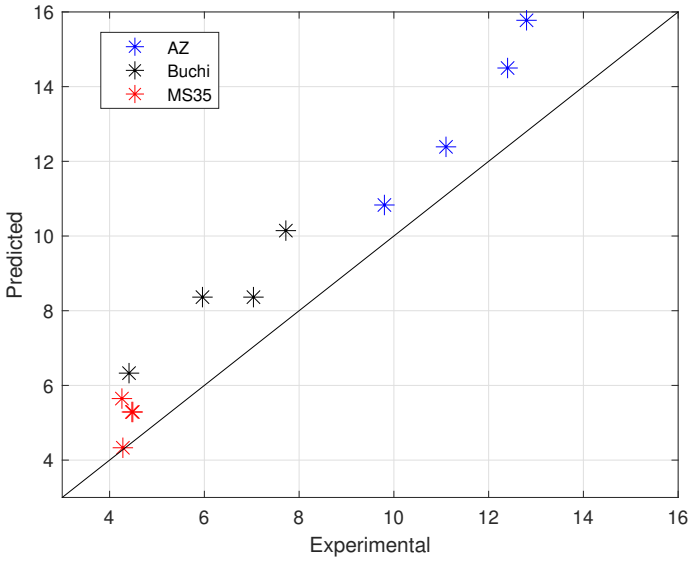

Figure 4.20: DS Parameter estimation of $D_{constant,A}$ predicting SSA

From the trend of major iterations of the model validation for both variables in a single experiment, it could be seen that the major iterations were much fewer and the control seemingly worse for the diffusion factor.

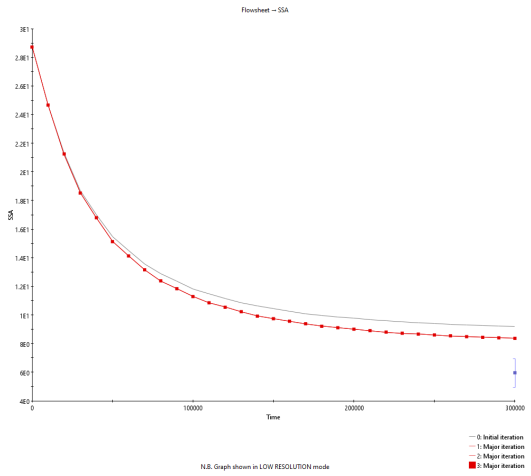

Figure 4.21

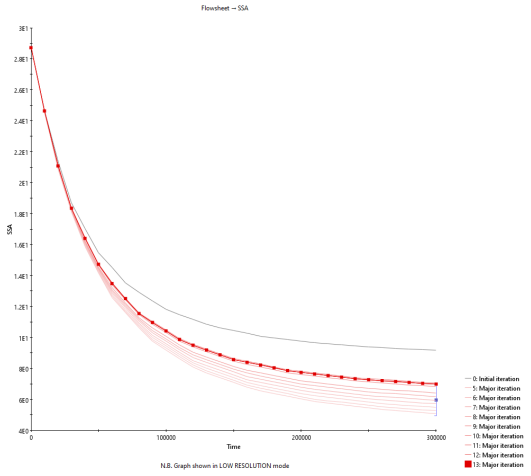

Figure 4.22: Main iterations critical concentration

Therefore to assess the influence the diffusion factor had on the system and to track what was driving crust formation on throughout the droplet sizes, simulations were performed on a single experiment (assumed represensentative of all the others) with the diffusion coefficient value from the parameter estimation and with the unaltered system. The results showed that excipient A still was the component forming the crust, and that the time until critical concentration was similar. The relative difference in real time (with the Stokes-Einstein diffusion case as reference) to reach critical concentration was roughly -6%, i.e. it took longer time to reach crust formation.
The influence of the diffusion factor upon the system was also examined with analytical equations describing the radial distribution of components valid for Pe<20 derived from the VFL model in [1, 23].
The experiment (said to be representative) was simulated using the parameter estimated diffusion factor, from table 4.3. Evaluating Peclet number at the constant drying stage, the value obtained is nearing zero.
Considering equation 2.32 from the theory section,

$$E_i = \frac{C_{s,i}}{C_{m,i}} = 1 + \frac{Pe_i}{5} + \frac{Pe_i^2}{100} - \frac{Pe_i^3}{4000}$$

at the limit when $Pe_i \to 0$ the surface enrichment $E_i \approx 1$. In equation 2.34, (also from theory section)

$$\tau_{sat,i} = \tau_D \left(1 - (S_{0,i} E_i)^{\frac{2}{3}}\right)$$

this mean that the influence of diffusion on the time of saturation diminishes when diffusion is set larger, which is why the diffusion constant from the parameter estimation has low impact of the system (diffusion coefficient is not able to capture droplet to particle transition). The takeaway from these results is that the concentration of the component of interest will be best for control, as the system is more sensitive to concentration and is why this is a good fitting parameter (critical concentration is able to describe onset of shell formation).
In simulations of separate experiments it was also discovered that the measurement time in the parameter estimation was set too low for the larger droplets within the system to dry. Running the experiment until complete drying showed that the relative difference of the SSA value (with the complete drying case with the parameter estimated C_{crit} as reference) was high, the parameter estimation gave an SSA that was 21 % higher.

4.6.1 Possible implications

The parameter estimation using a small subset of experiments across spray dryer scales suggest that estimation of critical concentration is scale independent and that it could be used for technology transfer across spray dryer systems. The strategy derived in this work could possibly be used to derive new information of systems/-formulations at small scale for new API. Also, the model built in this work could be implemented in the digital twin process library for the entire spray drying unit, aiding further research.

5
Conclusion

The ultimate goal of this thesis was to implement a mechanistic spray drying model that could account for key phenomena regarding particle formation in gPROMS. Also, evaluate the possibility to support derivation of critical process and formulation parameters with the model, that could ultimately develop new formulations and enable technology transfer.

The spray drying model was built as a hierarchical composite model within gPROMS, using model components. The 'Drying model' described single droplet drying (using Maxwell diffusion model as foundation) with heat and mass balances and internal radial distribution of solutes. Using an overall model, the drying model was coupled with an atomization model to calculate simultaneous multidroplet drying from size distribution. Each droplet/particle heat and mass balances were coupled to the spray drying environment via spray dryer thermodyanamics using a CSTR model.

Implementation of the spray drying model in gPROMS showed that the governing equations needed to be nondimensionalized to numerically handle the small time and length scales of spray drying systems for inhaled powders. Reformulation of the equations also resulted in a more robust and quick model. From model verification with an in house model, it was shown that the constructed model had good agreement in critical process parameters from eg. the time to reach critical concentration and complete drying of pure solvent droplet. The core focus of the work was to create a spray drying model using model components to predict shell formation, which ultimately could be used to estimate critical parameters for onset of shell formation such as eg. critical concentration and diffusion coefficient.

The model was validated with experimental data of large water droplet drying, showing excellent predictions. From sensitivity analysis it was shown that the diffusion coefficient defined from a literature value and by Stokes-Einstein gave similar surface concentration trajectories. This result made it possible to use either diffusion coefficient description within the model for shell formation predictions. Droplet size distribution and the quantiles from the log-normal cumulative distribution were found to follow the derived d_{10}, d_{50} and d_{90} from regression in a fair manner. For each dryer the heat loss was estimated, showing good predictability of the exhaust temperature.

In the parameter estimation it was deducted together with the analytical expression of the time to reach saturation from the 'VFL' model that the diffusion coefficient

(within reasonable ranges) had minor impact on the system. On the other hand, the critical concentration was found suitable as control variable as the results of parameter estimation were consistent for both cases (without and with modification of the other components respective critical concentration and diffusion). It was also concluded that the measurement time inside the parameter estimation was too short for the droplets of the larger sizes to reach critical concentration. However, due to time constraint and issues with implementing a simulation dependent measurement time this was not rectified.

Using model validation tool in gPROMS, by fitting to a limed dataset (4 experiments for each dryer type), the model was able to estimate critical concentration to determine onset of shell formation. From external validation, the estimation was shown to be robust and consistent across spray dryer scales and formulation compositions. To conclude, the results suggest there is potential of using the strategy derived from this work to support formulation development and technology transfer within the inhalation area.

5.1 Further development

5.1.1 Diffusion and mobility

It is clear that there isn't a major difference between the results attained of surface concentration from the diffusion coefficient taken from literature and the Stokes-Einstein equation, see figure 4.8. Also, from the parameter estimation and analysis with the analytical VFL solution, the overall effect and impact of the diffusion (evaluated within reasonable ranges) on shell formation was shown to be low. Since the influence of diffusion was low, it is likely that some other physical phenomena describing mobility of solutes is dominant, i.e. more capable of describing shell formation. With this background, it is reasonable to hypothesise that a viscosity increase which stem from an increased solid content (lower moisture content) close to the surface play a significant role describing the mobility of solute components and is decisive for shell formation and final radial distribution.

There are considerably few model studies of the internal structure development of spray dried particles in comparison to those describing the shell formation due to high concentration buildup at the liquid droplet surface [22]. It is logical that shell formation is initiated at the surface. However, quantification of interactions with the subsurface such as possible secondary shell formers, due to change in plasticity, surface activity and/or motion of components by their amphiphilic nature might be necessary to improve the prediction of the radial distribution. As stated in the theory surface affinity is probably one of the largest problems left to tackle concerning the description of solute mobility.

5.1.2 Model improvement

5.1.2.1 Single droplet drying model

In order to save resources when performing parameter estimation it might be possible to find a cutoff time where some larger droplets are still drying and still attain a good approximation of the SSA. The reason behind this is that larger droplets won't contribute that much to the total SSA as small droplets, because they have a smaller area to volume ratio as well as the number of droplets within these sizes are small when comparing to the amount of droplets with smaller sizes in the PSD.
To enable better more physico-chemically grounded predictions of the control variable SSA for parameter estimation it might be necessary to include effects of the shell on the mass transfer of solvent. Naturally as the shell is created the mass transfer should be inhibited by the crust and the effects becomes larger as the solute deposits on the inside of the shell as the solvent moves from the core to the liquid-solid interface. It would also be necessary to explain the change in permeability and/or porosity with the increased shell thickness. A potential improvement could be the application of a similar mass transfer resistance such described by Nešić and Vodnik [14], or a shrinking core model.
In addition there needs to be a quantitive way to describe the effects the morphological development has on the area of the particle. It is an unlikely scenario that the area can be assumed to be described by a perfect sphere. By the same logic, describing a phenomena such as buckling via ideal particle shrinkage is problematic. Perhaps it would be possible to semi-empirically correlate the ideal spherical area to some experimental results of shape. Another potential solution could be describing local moisture content within the shell and the capillary forces induced by drying. Where the effects of non-evaporating particle at the end of drying also should be added.

5.1.2.2 Dryer model

The CSTR was chosen to model spray dryer thermodynamics with supporting data from CFD from a similar system. To evaluate the actual flow implications on the single droplet drying model such as the temperature profile within the spray dryer body and the droplet/particle residence time the PFR flow model should be used instead. The PFR model would also enable examination of the impact the high temperature region close to the atomizer nozzle has on particle formation.

Bibliography

[1] Vehring R. *Pharmaceutical particle engineering via spray drying*. May 2008. DOI: 10.1007/s11095-007-9475-1.

[2] Karolinska Institutet. *Svensk MeSH - Asthma*. Last accessed 25 January 2023. 2022. URL: https://mesh.kib.ki.se/term/D001249/asthma.

[3] Levy M. L. et al. "Understanding Dry Powder Inhalers: Key Technical and Patient Preference Attributes." In: *Advances in therapy* 36.10 (2019), pp. 2547–2557.

[4] Elversson J. "Spray-Dried Powders for inhalation. Particle Formation and Formulation Concepts." PhD thesis. Uppsala University, 2005.

[5] Al Zaitone B et al. "Spray Drying of PEG6000 Suspension: Reaction Engineering Approach (REA) Modeling of Single Droplet Drying Kinetics". In: *Processes* 10.7 (July 2022). ISSN: 22279717. DOI: 10.3390/pr10071365.

[6] Patel K et al. "One-dimensional simulation of co-current, dairy spray drying systems - Pros and cons". In: *Dairy Science and Technology*. Vol. 90. 2-3. Mar. 2010, pp. 181–210. DOI: 10.1051/dst/2009059.

[7] Muzammil A. *Numerical Modelling of a Counter-Current Spray Drying Tower*. Tech. rep. 2014.

[8] Lowinger M et al. "Practical Considerations for Spray Dried Formulation and Process Development. In: Templeton, A., Byrn, S., Haskell, R., Prisinzano, T. (eds) Discovering and Developing Molecules with Optimal Drug-Like Properties." In: 15 (2015). DOI: 10.1007/978-1-4939-1399-2_12.

[9] Vicente J et al. "Fundamental analysis of particle formation in spray drying". In: *Powder Technology* 247 (Oct. 2013), pp. 1–7. ISSN: 00325910. DOI: 10.1016/j.powtec.2013.06.038.

[10] Nandiyanto A.B.D and Okuyama K. "Progress in developing spray-drying methods for the production of controlled morphology particles: From the nanometer to submicrometer size ranges". In: *Advanced Powder Technology* 22.1 (2011), pp. 1–19. ISSN: 15685527. DOI: 10.1016/j.apt.2010.09.011.

[11] Boel E et al. *Unraveling particle formation: From single droplet drying to spray drying and electrospraying*. July 2020. DOI: 10.3390/pharmaceutics12070625.

[12] Keey R. B. *Drying of Loose and Particulate Materials*. Vol. 10. 4. Taylor Francis, 1992, pp. 1139–1141. DOI: 10.1080/07373939208916507.

[13] Huang D. *European Drying Conference-EuroDrying*. Tech. rep. 2011, pp. 26–28.

[14] Nešić S and Vodnik J. "Kinetics of droplet evaporation". In: *Chemical Engineering Science* 46.2 (1991), pp. 527–537. ISSN: 0009-2509. DOI: 10.1016/

0009-2509(91)80013-O. URL: https://www.sciencedirect.com/science/article/pii/000925099180013O.

[15] Dobry D. E., D. M. Settell, and Baumann J. M. "A Model-Based Methodology for Spray-Drying Process Development". In: *J Pharm Innov* 4 (2009), pp. 133–142. DOI: 10.1007/s12247-009-9064-4.

[16] Crowder T. M. et al. "Fundamental effects of particle morphology on lung delivery: predictions of Stokes' law and the particular relevance to dry powder inhaler formulation and development". In: *Pharmaceutical research* 19 (2002), pp. 239–245. DOI: 10.1023/a:1014426530935.

[17] Rogers S et al. "Particle shrinkage and morphology of milk powder made with a monodisperse spray dryer". In: *Biochemical Engineering Journal* 62 (Mar. 2012), pp. 92–100. DOI: 10.1016/j.bej.2011.11.002.

[18] Karlsson S et al. "Characterization and mathematical modelling of single fluidised particle coating". In: *Powder Technology* 207.1-3 (Feb. 2011), pp. 245–256. DOI: 10.1016/j.powtec.2010.11.006.

[19] Nijdam J. J. and Langrish T. A.G. "The effect of surface composition on the functional properties of milk powders". In: *Journal of Food Engineering* 77.4 (Dec. 2006), pp. 919–925. ISSN: 02608774. DOI: 10.1016/j.jfoodeng.2005.08.020.

[20] Ratner B. D. and Castner D. G. "Electron Spectroscopy for Chemical Analysis". In: *Surface Analysis – The Principal Techniques*. John Wiley Sons, Ltd, 2009. Chap. 3, pp. 47–112. ISBN: 9780470721582. DOI: https://doi.org/10.1002/9780470721582.ch3.

[21] Faldt P, Bergenstahl B, and Carlsson G. "The Surface Coverage of Fat on Food Powders Analyzed by Esca (Electron Spectroscopy for Chemical Analysis)". In: *Food Structure* 12.2 (). URL: https://digitalcommons.usu.edu/foodmicrostructure/vol12/iss2/10.

[22] Chen X. D, Sidhu H, and Nelson M. "Theoretical probing of the phenomenon of the formation of the outermost surface layer of a multi-component particle, and the surface chemical composition after the rapid removal of water in spray drying". In: *Chemical Engineering Science* 66.24 (2011). Novel Gas Conversion Symposium- Lyon 2010, C1-C4 Catalytic Processes for the Production of Chemicals and Fuels, pp. 6375–6384. ISSN: 0009-2509. DOI: 10.1016/j.ces.2011.08.035. URL: https://www.sciencedirect.com/science/article/pii/S000925091100604X.

[23] Vehring R, Foss W. R., and Lechuga-Ballesteros D. "Particle formation in spray drying". In: *Journal of Aerosol Science* 38.7 (2007), pp. 728–746. ISSN: 00218502. DOI: 10.1016/j.jaerosci.2007.04.005.

[24] Eijkelboom N. M. et al. "Particle structure development during spray drying from a single droplet to pilot-scale perspective". In: *Journal of Food Engineering* 337 (2023), p. 111222. ISSN: 0260-8774. DOI: 10.1016/j.jfoodeng.2022.111222. URL: https://www.sciencedirect.com/science/article/pii/S026087742200276X.

[25] Vasudevan S. "Modeling of multiphase flows in a spray dryer". Available at https://odr.chalmers.se/items/2ea53b62-ae23-472c-9ba2-

ac773f1606e1. Master's thesis. Göteborg, Sweden: Chalmers University of Technology, 2020.

[26] Mezhericher M, Levy A, and Borde I. "Modelling of particle breakage during drying". In: *Chemical Engineering and Processing: Process Intensification* 47.8 (2008), pp. 1404–1411. ISSN: 02552701. DOI: 10.1016/j.cep.2007.06.018.

[27] Sugiyama Y et al. "Buckling and Crumpling of Drying Droplets of Colloid-Polymer Suspensions". In: *Langmuir* 22.14 (2006). PMID: 16800655, pp. 6024–6030. DOI: 10.1021/la053419h.

[28] Tsapis N et al. "Onset of Buckling in Drying Droplets of Colloidal Suspensions". In: *Phys. Rev. Lett.* 94 (1 Jan. 2005), p. 018302. DOI: 10.1103/PhysRevLett.94.018302.

[29] Pardeshi S et al. "A meticulous overview on drying-based (spray-, freeze-, and spray-freeze) particle engineering approaches for pharmaceutical technologies". In: *Drying Technology* 39.11 (2021), pp. 1447–1491. DOI: 10.1080/07373937.2021.1893330.

[30] Langrish T. A. G. and Kockel T. K. *The assessment of a characteristic drying curve for milk powder for use in computational fluid dynamics modelling*. Tech. rep. 2001, pp. 69–74.

[31] de Souza Lima R, Ré M.-I., and Arlabosse P. "Drying droplet as a template for solid formation: A review". In: *Powder Technology* 359 (2020), pp. 161–171. ISSN: 0032-5910. DOI: 10.1016/j.powtec.2019.09.052. URL: https://www.sciencedirect.com/science/article/pii/S0032591019308010.

[32] George O. A. et al. "An effective rate approach to modeling single-stage spray drying". In: *AIChE Journal* 61.12 (Dec. 2015), pp. 4140–4151. ISSN: 15475905. DOI: 10.1002/aic.14940.

[33] Mezhericher M, Levy A, and Borde I. "Theoretical models of single droplet drying kinetics: A review". In: *Drying Technology* 28.2 (Feb. 2010), pp. 278–293. ISSN: 07373937. DOI: 10.1080/07373930903530337.

[34] Mezhericher M, Levy A, and Borde I. "Theoretical modelling and numerical simulation of spray drying processes". In: (Jan. 2014).

[35] Harvie D.J.E., Langrish T.A.G., and Fletcher D.F. "A Computational Fluid Dynamics Study of a Tall-Form Spray Dryer". In: *Food and Bioproducts Processing* 80.3 (2002), pp. 163–175. ISSN: 0960-3085. DOI: https://doi.org/10.1205/096030802760309188. URL: https://www.sciencedirect.com/science/article/pii/S0960308502703167.

[36] Fyhr C and Kemp I. C. "Comparison of different drying kinetics models for single particles". In: *Drying Technology* 16.7 (1998), pp. 1339–1369. DOI: 10.1080/07373939808917465.

[37] Chen X.D. and Xie G.Z. "Fingerprints of the Drying Behaviour of Particulate or Thin Layer Food Materials Established Using a Reaction Engineering Model". In: *Food and Bioproducts Processing* 75.4 (1997), pp. 213–222. ISSN: 0960-3085. DOI: 10.1205/096030897531612. URL: https://www.sciencedirect.com/science/article/pii/S0960308597700786.

[38] Nan Fu et al. "Reaction Engineering Approach (REA) to model the drying kinetics of droplets with different initial sizes-experiments and analy-

ses". In: *Chemical Engineering Science* 66.8 (Apr. 2011), pp. 1738–1747. ISSN: 00092509. DOI: 10.1016/j.ces.2011.01.009.

[39] Chen X.D. and Putranto A. *Modelling Drying Processes - A Reaction Engineering Approach*. Cambridge University Press, 2013. DOI: 10.1017/CBO9780511997846.

[40] Boraey M.A. and Vehring R. *Diffusion controlled formation of microparticles*. 2014. DOI: 10.1016/j.jaerosci.2013.10.002.

[41] Ordoubadi M et al. "Multi-Solvent Microdroplet Evaporation: Modeling and Measurement of Spray-Drying Kinetics with Inhalable Pharmaceutics". In: *Pharmaceutical Research* 36.7 (July 2019). ISSN: 1573904X. DOI: 10.1007/s11095-019-2630-7.

[42] Finlay W H. "4 - Particle size changes due to evaporation or condensation". In: *The Mechanics of Inhaled Pharmaceutical Aerosols*. London: Academic Press, 2001, pp. 47–91. ISBN: 978-0-12-256971-5. DOI: 10.1016/B978-012256971-5/50005-5. URL: https://www.sciencedirect.com/science/article/pii/B9780122569715500055.

[43] Sirignano W. A. and Wu G. "Multicomponent-liquid–fuel vaporization with complex configuration". In: *International Journal of Heat and Mass Transfer* 51.19 (2008), pp. 4759–4774. ISSN: 0017-9310. DOI: 10.1016/j.ijheatmasstransfer.2008.02.018. URL: https://www.sciencedirect.com/science/article/pii/S0017931008001257.

[44] Handscomb C.S. and Kraft M. "Simulating the structural evolution of droplets following shell formation". In: *Chemical Engineering Science* 65.2 (2010), pp. 713–725. ISSN: 0009-2509. DOI: 10.1016/j.ces.2009.09.025. URL: https://www.sciencedirect.com/science/article/pii/S0009250909006198.

[45] Montgomery D. C. *Design and Analysis of Experiments 8th Ed.* John Wiley Sons Singapore Pte. Ltd., 2013.

[46] Siemens Process Systems Engineering Limited. *gPROMS FormulatedProducts Documentation*. July 2022.

[47] Process Systems Enterprise Limited. *gPROMS Introductory User Guide*. June 2004.

[48] Sirignano W.A. *Fluid dynamics and transport of droplets and sprays*. Cambridge University Press, 1999. DOI: 10.1017/CBO9780511529566.

[49] Welty J R, Rorrer G L, and Foster D G. *Fundamentals of Momentum, Heat and Mass Transfer*. John Wiley Sons Singapore Pte. Ltd., 2015. ISBN: 978-1-118-80887-0.

[50] van der Lijn J. "Simulation of heat and mass transfer in spray drying". In: 1976.

[51] Moors J.J.A., Strijbosch L.W.G., and van Groenendaal W.J.H. *Estimating Mean and Variance Through Quantiles: An Experimental Comparison of Different Methods*. WorkingPaper. Operations research, 2002.

[52] MathWorks. *MathWorks Help Center - Lognormal Distribution*. Last accessed 14 June 2023. 2023. URL: https://se.mathworks.com/help/stats/lognormal-distribution.html.

[53] Roache P. J. "Perspective: A Method for Uniform Reporting of Grid Refinement Studies". In: *Journal of Fluids Engineering* 116.3 (Sept. 1994), pp. 405–413. ISSN: 0098-2202. DOI: 10.1115/1.2910291.

[54] NASA. *NPARC Alliance CFD Verification and Validation Web Site - Examining Spatial (Grid) Convergence*. Last accessed 17 May 2023. 2021. URL: https://www.grc.nasa.gov/WWW/wind/valid/tutorial/spatconv.html.

[55] Celik I. B. et al. "Procedure for Estimation and Reporting of Uncertainty Due to Discretization in CFD Applications". In: 2007.

[56] Mörtstedt S. G. and Hellsten G. *Data och Diagram Energi- och kemitekniska tabeller*. Liber AB, 2016.

[57] Langrish T.A.G. "Book Review: Drying of Loose and Particulate Materials". In: (2007). DOI: 10.1080/07373939208916507.

[58] NIST. *NIST Chemistry WebBook, SRD 60 - Nitrogen - Gas Phase Heat Capacity (Shomate equation)*. Last accessed 14 June 2023. 2023. URL: https://webbook.nist.gov/cgi/cbook.cgi?ID=C7727379&Type=JANAFG&Plot=on.

[59] Henderson-Sellers B. "A new formula for latent heat of vaporization of water as a function of temperature". In: *Quarterly Journal of the Royal Meteorological Society* 110.466 (1984), pp. 1186–1190. DOI: 10.1002/qj.49711046626. URL: https://rmets.onlinelibrary.wiley.com/doi/abs/10.1002/qj.49711046626.

[60] Marrero T. R. and Mason E. A. "Gaseous Diffusion Coefficients". In: *Journal of Physical and Chemical Reference Data* 1.1 (Oct. 2009), pp. 3–118. ISSN: 0047-2689. DOI: 10.1063/1.3253094. eprint: https://pubs.aip.org/aip/jpr/article-pdf/1/1/3/12134358/3_1_online.pdf.

[61] Stephan K and Laesecke A. "The Thermal Conductivity of Fluid Air". In: *Journal of Physical and Chemical Reference Data* 14.1 (Jan. 1985), pp. 227–234. ISSN: 0047-2689. DOI: 10.1063/1.555749. eprint: https://pubs.aip.org/aip/jpr/article-pdf/14/1/227/9766451/227_1_online.pdf.

[62] NIST. *NIST Chemistry WebBook, SRD 60 - Water - Antoine Equation Parameters*. Last accessed 14 June 2023. 2023. URL: https://webbook.nist.gov/cgi/cbook.cgi?ID=C7732185&Mask=4.

[63] Kestin J, Sokolov M, and Wakeham W. A. "Viscosity of liquid water in the range 8°C to 150°C". In: *Journal of Physical and Chemical Reference Data* 7.3 (July 1978), pp. 941–948. ISSN: 0047-2689. DOI: 10.1063/1.555581. eprint: https://pubs.aip.org/aip/jpr/article-pdf/7/3/941/12153354/941_1_online.pdf.

[64] Pátek J et al. "Reference Correlations for Thermophysical Properties of Liquid Water at 0.1MPa". In: *Journal of Physical and Chemical Reference Data* 38.1 (Jan. 2009), pp. 21–29. ISSN: 0047-2689. DOI: 10.1063/1.3043575. eprint: https://pubs.aip.org/aip/jpr/article-pdf/38/1/21/16675584/21_1_online.pdf.

A

Appendix 1

A.1 Nondimensionalized model equations

The variables used in the equations are summarized in table A.1. Where the characteristic dimensions are length L (m), mass M (kg), time t (s), temperature T (K) and enthalpy H (J).

Table A.1: Variables involved in the model

Variable	Physical property	Characteristic dimension	SI
m	mass	M	kg
Cp_l	specific heat	$HM^{-1}T^{-1}$	J/kgK
T	temperature	T	K
k	thermal conductivity	$HL^{-1}T^{-1}t^{-1}$	J/smK
L_v	enthalpy of vaporization	HM^{-1}	J/kg
C	concentration	ML^{-3}	kg/m3
d	diameter	L	m
D	diffusion	L^2t^{-1}	m2/s
t	time	t	s
ρ	density	ML^{-3}	kg/m3

To non-dimensionalize the system of equations the time, mass and length were converted into dimensionless variables as

$$\tilde{t} = \frac{t}{t_s}; \tilde{m} = \frac{m}{m_s}; \tilde{d} = \frac{d}{d_s} \tag{A.1}$$

using

$$t_s = \frac{d_0^2}{D}; m_s = \frac{\rho \pi d0^3}{6}; d_s = d_0. \tag{A.2}$$

Where D is the diffusion of water vapor in nitrogen gas.

A.1.1 Energy

From equation describing the heat balance,

$$mCp_l \frac{dT_d}{dt} = -2\pi kd(T_d - T_{gas}) + \Delta H_{vap} \frac{dm}{dt} \tag{A.3}$$

converting to dimensionless time and mass gives

$$\frac{m_s \tilde{m} Cp_l}{t_s}\frac{dT_d}{d\tilde{t}} = -2\pi k(T_d - T_{gas}) + \Delta H_{vap}\frac{m_s}{t_s}\frac{d\tilde{m}}{d\tilde{t}}. \tag{A.4}$$

using the newly defined t_s, m_s and d_s leads to

$$\frac{dT_d}{d\tilde{t}} = \frac{-12k\tilde{d}(T_d - T_{gas})}{\tilde{m}\rho DCp_l} + \frac{\Delta H_{vap}}{\tilde{m}Cp_l}\frac{d\tilde{m}}{d\tilde{t}}. \tag{A.5}$$

Identifying Lewis number

$$Le = \frac{k}{\rho DC_p} \tag{A.6}$$

and rewriting A.5

$$\frac{dT_d}{d\tilde{t}} = \frac{-12L_e\tilde{d}(T_d - T_{gas})}{\tilde{m}} + \frac{\Delta H_{vap}}{\tilde{m}Cp_l}\frac{d\tilde{m}}{d\tilde{t}} \tag{A.7}$$

Using that $\tilde{m}$,

$$\tilde{m} = \frac{d^3}{d_0^3} = \tilde{d^3} \tag{A.8}$$

into A.7 and simplifying gives

$$\frac{dT_d}{d\tilde{t}} = \frac{-12L_e(T_d - T_{gas})}{\tilde{d^2}} + \frac{\Delta H_{vap}}{\tilde{d^3}Cp_l}\frac{d\tilde{m}}{d\tilde{t}} \tag{A.9}$$

A.1.2 Mass

From the mass balance

$$\frac{dm}{dt} = -2\pi dD(C_s - C_\infty) \tag{A.10}$$

gives the left hand side as

$$\frac{m_s}{t_s}\frac{d\tilde{m}}{d\tilde{t}} = \frac{\frac{\rho\pi d^3}{6}}{\frac{d_0^2}{D}}\frac{d\tilde{m}}{d\tilde{t}} \tag{A.11}$$

writing out and simplifying leads to

$$\frac{d\tilde{m}}{d\tilde{t}} = -\frac{12\tilde{d}}{\rho}(C_s - C_\infty) \tag{A.12}$$

A.1.3 Size

$$\frac{dd}{dt} = -\frac{4D(C_s - C_\infty)}{\rho d} \tag{A.13}$$

In non-dimensionalized terms

$$\frac{d\tilde{d}}{d\tilde{t}} = -\frac{4(C_s - C_\infty)}{\rho\tilde{d}} \tag{A.14}$$

A.1.4 Internal radial distribution of solutes

From the radial distribution of component concentration in SI units,

$$\frac{\partial C_j}{\partial t} = \frac{4D_j}{d^2}\left(\frac{\partial^2 C_j}{\partial R^2} + \frac{2}{R}\frac{\partial C_j}{\partial R}\right) - \frac{\kappa R}{2d^2}\frac{\partial C_j}{\partial R} \tag{A.15}$$

By the d^2 law κ is defined as

$$\frac{dd^2}{dt} = -\kappa \tag{A.16}$$

which in dimensionless terms leads to 'Peclet' number, observe that this is not the same as the earlier definition of Pe in theory as D is the diffusion of water vapor in nitrogen and not the internal diffusion coefficient.

$$\frac{d\tilde{d}^2}{d\tilde{t}} = -\frac{\kappa}{D} = -Pe. \tag{A.17}$$

Non-dimensionalizing A.15 just in the time dimension gives after simplification

$$\frac{\partial C_j}{\partial \tilde{t}} = \frac{4D_j}{\tilde{d}^2 D}\left(\frac{\partial^2 C_j}{\partial R^2} + \frac{2}{R}\frac{\partial C_j}{\partial R}\right) - \frac{PeR}{2\tilde{d}^2}\frac{\partial C_j}{\partial R} \tag{A.18}$$

The initial and boundary conditions for the radial distribution do not change and are the same as in section 2.1.2.3.

A.2 Matlab Curve fitter

A.2.1 X, moisture content solid kg wet/kg dry

Linear model Poly1: X = p1·ϕ + p2; (kg wet / kg dry)
Coefficients (with 95% confidence bounds):
p1 = 0.2455 (0.232, 0.2589)
p2 = 0.003576 (-0.0026, 0.009752)
Goodness of fit:
SSE: 3.692e-05
R-square: 0.9991
Adjusted R-square: 0.9988
RMSE: 0.003508

A.2.2 P_{sat}

Linear model Poly4:
with T in degree celcius
P_{sat} = p1·T^4 + p2·T^3 + p3·T^2 + p4·T + p; (Pa)
Coefficients (with 95% confidence bounds):
p1 = 0.0009656 (0.0009002, 0.001031)
p2 = -0.03331 (-0.0465, -0.02012)
p3 = 3.552 (2.695, 4.409)

p4 = 18.75 (-0.8057, 38.31)
p5 = 643.2 (516.2, 770.2)

Goodness of fit:
SSE: 1.765e+04
R-square: 1
Adjusted R-square: 1
RMSE: 54.23

A.3 Grid evaluation

All simulations in the grid evaluation was performed using the intial droplet size of 52 μm, inlet feed temperature and gas temperature as 20°C. The solid loading was either excipient A or B, the initial concentrations used were ■ and ■ mg/ml respectively.

A.3.1 Excipient A

Table A.2: Simulation with non-uniform grid with excipient A, SI model

Grid points	$t_{simulation}$ (s)	CPU (s)	$t_{C_{crit}}$ (s)	diameter (μm)
10	37.7	36.5	1.65853	25.8623
100	81.9	81.4	1.65975	25.8335
1000	1558.0	1556.3	1.65977	25.8331

The transformation coefficient a = 4.

Table A.3: Simulation with non-uniform grid with excipient A, Non-dimensionalized model

Grid points	$t_{simulation}$ (s)	CPU (s)	$t_{C_{crit}}$ (s)	diameter (μm)
10	1.5	0.3	1.65972	25.9000
100	1.0	0.9	1.66095	25.8335
1000	14.4	14.2	1.66096	25.8332
10000	160.9	158.8	1.66096	25.8332

The transformation coefficient a = 4.

Table A.4: Simulation with non-uniform grid with excipient A, Non-dimensionalized model

Grid points	a	$t_{simulation}$ (s)	CPU (s)	$t_{C_{crit}}$ (s)	diameter (μm)
100	4	1.0	0.9	1.66095	25.8335
100	5	1.0	0.8	1.66093	25.8340
100	6	1.0	0.9	1.66086	25.8355

Table A.4 shows a comparison between the same grid point configuration, but different transformation coefficients. The in-house model with the same process conditions and feed formulation gave, $t_{c_{crit}} = 1.7909$ s and $t_{simulation} = 25.6782$ s.

A.3.2 Excipient B

Table A.5: Simulation with uniform grid with excipient B, SI based model

Grid points	$t_{simulation}$ (s)	CPU (s)	$t_{C_{crit}}$ (s)	diameter (μm)
10	11.1	9.9	1.75912	23.3889
100	37.4	36.1	1.76037	23.3566
1000	696.4	695.7	1.76037	23.3564

Table A.6: Simulation with uniform grid with excipient B, Nondimensionalized model

Grid points	$t_{simulation}$ (s)	CPU (s)	$t_{C_{crit}}$ (s)	diameter (μm)
10	1.5	0.3	1.75415	23.5480
100	0.8	0.7	1.75583	23.5047
1000	10.6	10.4	1.75584	23.5044
10000	14.5	14.0	1.75584	23.5044

A.4 Model validification equations for parameter estimation of heat loss

A.4.1 Drying without solids

$$\begin{aligned}\dot{m}_{ag}Cp_{ag}T_{in,ag} + \dot{m}_{dg}Cp_{dg}T_{in,dg} = {} & \dot{m}_{ag}Cp_{ag}(1+Y_{ag})T_{out} \\ & + \dot{m}_{dg}Cp_{dg}(1+Y_{dg})T_{out} \\ & + \dot{m}_{feed}\Big\{Cp_{water,liq}(T_{evap} - T_{in,feed}) \\ & + \Delta H_{vap} + Cp_{water,gas}(T_{out} - T_{evap})\Big\} \\ & + \text{Heat loss}\end{aligned} \tag{A.19}$$

A.4.2 Drying with solids

$$\begin{aligned}\dot{m}_{ag}Cp_{ag}T_{in,ag} + \dot{m}_{dg}Cp_{dg}T_{in,dg} = \dot{m}_{ag}Cp_{ag}T_{out} + \dot{m}_{dg}Cp_{dg}T_{out} \\ + \dot{m}_{solid}\Big\{(X_{in} - X_{out})(Cp_{water,liq}(T_{evap} - T_{in}) \\ + Cp_{water,vap}(T_{out} - T_{evap}) + \Delta H_{vap}\Big\} \\ + \dot{m}_{solid}(Cp_{solid} + X_{out}Cp_{water,liq})(T_{out} - T_{in}) \\ + \text{Heat loss}\end{aligned} \tag{A.20}$$

Where heat loss for both A.19 and A.20 is defined as

$$\text{Heat loss} = h_{pipe}(T_{in,dg} - T_{amb}) + h_{body}(T_{out} - T_{amb}) \tag{A.21}$$

A.5 gPROMS code

A.6 Transport phenomena coefficients

Applying boundary-theory approximation necessitates transport coefficients being evaluated at the specific boundary state. Seen from earlier works this overall model is based upon the results of the corresponding authors models fit best to experimental data by evaluating transport coefficients at $T_{intermediate}$ which is 1/3 of the gas temperature and 2/3 of the droplet temperature, the "one third rule" is applied [23, 41].

$$T_{intermediate} = \frac{2}{3}T_{droplet} + \frac{1}{3}T_{gas} \tag{A.22}$$

Since diffusion within the drying gas is much quicker than in liquid, the drying gas is assumed to be in a quasi-steady state with regards to the droplet/particle [48].

A.6.1 Nitrogen heat capacity [58]

Valid for range 100 - 500K.

$$Cp = A + Bt + Ct^2 + Dt^3 + \frac{E}{t^2} \tag{A.23}$$

Where t=temperature(K)/1000.
A=28.98641, B=1.853978, C=-9.647459, D=16.63537, E=0.000117

A.6.2 Latent heat of vaporization of water [59]

Valid for range 273 - 323K.

$$L = 1.91846 \cdot 10^6 \cdot \left(\frac{T}{T - 33.91}\right)^2 \text{ J/kg} \tag{A.24}$$

Where T is the temperature in K.

A.6.3 Diffusion coefficient of water vapor in nitrogen [60]

Valid for range 282 - 373K.

$$D = 1.87 \cdot T_{intermediate}^{2.072} \cdot 10^{-10} \quad \mathrm{m^2/s} \tag{A.25}$$

$T_{intermediate}$ (K) is taken from the one third rule.

A.6.4 Thermal conductivity of air [61]

Valid for range 70 - 1400K.

$$\lambda_{OR} = C_1 T_R^{-1} + C_2 T_R^{-2/3} + C_3 T_R^{-1/3} + C_4 + C_5 T_R^{1/3} + C_6 T_R^{2/3} + C_7 T_R + C_8 T_R^{4/3} + C_9 T_R^{5/3} \tag{A.26}$$

Where $\lambda_o(T)$ is the thermal conductivity of dilute air.
$\lambda_{OR} = \lambda_o/\Lambda, T_R = T/T_c$; $\Lambda = 4.358 \cdot 10^{-3}$ W/mK, T_c= 132.52K.
Dimensionless parameters C_i:
C_1 = 33.9729025, C_2 = -164.702679, C_3 = 262.108546, C_4 = -21.5346955,
C_5 = -443.455815 C_6 = 607.339582, C_7 = -368.790121, C_8 = 111.296674,
C_9 = -13.412246

A.6.5 Saturation vapor pressure, P_{sat} [62]

Antoine equation

$$log_{10}(P) = A - \frac{B}{T + C} \tag{A.27}$$

Where P is the vapor pressure (bar) and T is temperature (K). Coefficients taken from [62].

A.6.6 Viscosity of water [63]

Valid for range -8°C$\leq$ t $\leq$ 150°C.

$$log\left\{\frac{\mu(t)}{\mu(20°C)}\right\} = \frac{20-t}{t+96}\{1.2378 - 1.303\cdot10^{-3}(20-t) + 3.06\cdot10^{-6}(20-t)^2 + 2.55\cdot10^{-8}(20-t)^3\} \tag{A.28}$$

Where t is the temperature of the droplet in °C and $\mu(20°C) = 1002 \quad \mu Pas$.

A.6.7 Liquid water heat capacity [64]

Valid for range 253.15 - 383.15K. Isobaric heat capacity of liquid water at 0.1 MPa.

$$Cp_l = -R[c_3 + \tau\Sigma_{i=1}^{3} n_i(n_i+1)a_i\alpha^{n_i+2} + \tau\Sigma_{i=1}^{4} m_i(m_i+1)b_i\beta^{m_i+2}] \tag{A.29}$$

Where

$$\tau = \frac{T}{T_R}, \quad \alpha = \frac{T_R}{T_a - T}, \quad \beta = \frac{T_R}{T - T_b}$$

T is temperature in K, T_R = 10K, T_a= 593K, T_b = 232K, R = 461.51905 J/kgK.
Dimensionless coefficients a_i, b_i, c_i:
a_1 = -1.661470539 $\cdot 10^5$, a_2 = 2.708781640 $\cdot 10^6$, a_3 = -1.557191544 $\cdot 10^8$
b_1 = -8.237426256 $\cdot 10^{-1}$, b_2 = 1.908956353, b_3 = 8.546361348 $\cdot 10^{-1}$
c_3 = -8.983025854
With integer exponents n_i and m_i:
n_1 = 4, n_2 = 5, n_3 = 7
m_1 = 2 m_2 = 3 m_3 = 4 m_4 = 5

DEPARTMENT OF SOME SUBJECT OR TECHNOLOGY
CHALMERS UNIVERSITY OF TECHNOLOGY
Gothenburg, Sweden
www.chalmers.se

CHALMERS
UNIVERSITY OF TECHNOLOGY